

Washington University in St. Louis

Washington University Open Scholarship

McKelvey School of Engineering Theses & Dissertations

McKelvey School of Engineering

Summer 8-17-2017

Single-step, Atmospheric Pressure Chemical Vapor Deposition of Methylammonium Bismuth Iodide Thin Films

Xiao Chen

Washington University in St. Louis

Follow this and additional works at: https://openscholarship.wustl.edu/eng_etds



Part of the [Semiconductor and Optical Materials Commons](#)

Recommended Citation

Chen, Xiao, "Single-step, Atmospheric Pressure Chemical Vapor Deposition of Methylammonium Bismuth Iodide Thin Films" (2017). *McKelvey School of Engineering Theses & Dissertations*. 251.
https://openscholarship.wustl.edu/eng_etds/251

This Thesis is brought to you for free and open access by the McKelvey School of Engineering at Washington University Open Scholarship. It has been accepted for inclusion in McKelvey School of Engineering Theses & Dissertations by an authorized administrator of Washington University Open Scholarship. For more information, please contact digital@wumail.wustl.edu.

WASHINGTON UNIVERSITY IN ST. LOUIS

School of Engineering and Applied Science
Department of Mechanical Engineering and Materials Science

Thesis Examination Committee:
Parag Banerjee, Chair
Bryce Sadtler
Srikanth Singamaneni

Single-step, Atmospheric Pressure Chemical Vapor Deposition of Methylammonium Bismuth
Iodide Thin Films

by
Xiao Chen

A thesis presented to the School of Engineering
of Washington University in St. Louis in partial fulfillment of the
requirements for the degree of
Master of Science

August 2017

Saint Louis, Missouri

Contents

List of Figures	III
List of Tables	IV
List of Abbreviations	V
Acknowledgments	VI
ABSTRACT	VIII
1 Introduction	1
1.1 Motivation	1
1.2 Atmospheric Pressure Chemical Vapor Deposition	2
1.3 Synthesis Routes for Organic-inorganic Halide Thin Films	4
2 Materials and Experiments	8
2.1 Precursors Preparations	8
2.1.1 Methylammonium iodide preparation & characterization	8
2.1.2 Bismuth iodide preparation & characterization	9
2.2 Perovskite Synthesis via APCVD	10
2.3 Film Characterization	11
3 Bismuth Perovskites Synthesis via APCVD	13
3.1 APCVD process	13
3.2 Vapor Pressure Calculations	15
3.3 Mechanism of Film Deposition and Growth	19

3.4	Structure of MA ₃ Bi ₂ I ₉	24
3.5	Conclusions	28
4	Optical & Electrical Characterization	29
4.1	Optical Characterization.....	29
4.2	Electrical Characterization.....	31
4.3	Conclusion.....	33
5	Film Stability	34
5.1	Material Characterization.....	34
5.2	Optical & Electrical Characterizations	36
5.3	Conclusion.....	37
6	Conclusion	38
7	Future Work	39
	Appendix A	40
	Appendix B	50
	Appendix C	52
	Appendix D	54
	References	55
	Vita	60

List of Figures

Figure 1.1 Schematic representation of the fundamental transport and reaction steps underlying CVD ²⁰	3
Figure 2.1 XRD of MAI powder (black) with corresponding JCPDS file # 100737 in red below.....	9
Figure 3.1 (a) Schematic of APCVD for MA ₃ Bi ₂ I ₉ thin films, (b) Image of MAI and BiI ₃ boats inside the tube furnace and (c), temperature profile of the tube furnace showing the MAI and BiI ₃ sublimation temperatures and MA ₃ Bi ₂ I ₉ film deposition temperature.	14
Figure 3.2 : (a) TGA heating curves of the BiI ₃ precursor and (b) corresponding 1 st derivatives measured at different heating rates of BiI ₃ precursor; (c) calculated ln p vis 1/t of BiI ₃ precursor. (d) vapor pressure of BiI ₃ (black) and MAI (red) precursors as a function of temperature. The dotted vertical lines indicate the position where the MAI crucible (199 °C), BiI ₃ crucible (230 °C) and substrate (160 °C) are placed in the horizontal tube furnace.	18
Figure 3.3 SEM images of APCVD films for varying times of deposition. Scale bar = 500 nm.	20
Figure 3.4 Raman spectroscopy of BiI ₃ nanosheets. The Raman signal from SiO ₂ /Si substrate on which the BiI ₃ were deposited are as a comparison.	21
Figure 3.5 Schematic of deposition process mechanism in APCVD.....	21
Figure 3.6 Optical images of APCVD MA ₃ Bi ₂ I ₉ films on glass substrate for varying times of deposition. Arrow represents direction of Ar flow in the furnace. Scale bar = 1 cm.....	23
Figure 3.7 (a) Side view of MA ₃ Bi ₂ I ₉ film deposited twice for 360 minutes shows a thickness of 775 nm. (b) A repeat of MA ₃ Bi ₂ I ₉ film deposited for 360 minutes, eliminates these gaps and produces a dense, polycrystalline film. All optical and electrical measurements were performed on the 360 minutes (2×) sample.	24
Figure 3.8 (a) XRD of the MA ₃ Bi ₂ I ₉ films as a function of deposition time. Single crystal BiI ₃ reference is obtained from Boopathy et al., and is indexed with symbol ‘○’. MAI reference is obtained from JCPDS ref no. 000-10-0737 and is indexed with symbol ‘●’. MA ₃ Bi ₂ I ₉ reference is obtained from Abulikemu et al., and is indexed with symbol ‘■’. (b) Crystal structure of MA ₃ Bi ₂ I ₉ after relaxation along (100) (top) and (001) (bottom) crystallographic directions.	25
Figure 3.9 XPS fine spectra obtained from 15, 180 and 480 minute MA ₃ Bi ₂ I ₉ thin films showing (a) C 1s, (b) N 1s, (c) Bi 4f and, (d) I 3d. The carbon 1s peak has been deconvoluted into two peaks related to adventitious carbon (284.5 eV) and C-N from the methylammonium group.	27
Figure 4.1 (a) UV- vis spectra of MA ₃ Bi ₂ I ₉ film. (b) Exciton peak is extracted and a Tau ϵ plot of the baseline is used to measure the indirect bandgap ~ 2.08 eV (c) Cyclic voltammetry curve (vs. Ag/Ag+ electrode) for MA ₃ Bi ₂ I ₉ (d) Band edge information from experimental (UV-vis + CV)	30
Figure 5.1 (a) XPS fine spectra of N 1s shows absence of N after just 5 days exposure in ambient. (b) XPS fine spectra of I 3d for fresh, after 5 (no change) and 14 days in ambient. (c) XPS fine spectra of O 1s for fresh and after 5, 14 days in ambient. (d) XPS fine spectra of Bi 4f for fresh (black) and after 5(red) and 14 days (blue) in ambient.	35
Figure 5.2 (a) UV-vis spectra from day 0 (fresh) to day ‘5’ shows a gradual decay of the excitonic peak while insets show actual film fading color, and (b) Change in exciton peak intensity (black, left axis) and electrical resistivity (red, right axis) as a function of number of days exposed to ambient. The increase in resistivity follows a bi-exponential decay with time constants 0.1 and 1.7 days.....	36

List of Tables

Table 1 different process and resultant film properties	5
Table 2 The partial pressures obtained from thermogravimetric analysis of MAI and BiI ₃ powders.	17
Table 3 The enthalpy of sublimation (ΔH_{sub}) and sublimation temperature (T_{sub}) are shown for both the precursors	17
Table 4 XPS peak positions of N1s, Bi 4f _{7/2} and I 3d _{5/2} in the MA ₃ Bi ₂ I ₉ films deposited for 15, 180 and 480 minutes.....	28
Table 5 Comparison of Hall measurement data of MA ₃ Bi ₂ I ₉ films deposited using various synthesis techniques.....	32

List of Abbreviations

CVD = Chemical vapor deposition

APCVD = Atmospheric pressure chemical vapor deposition

MA₃Bi₂I₉ = Methylammonium bismuth iodide, (CH₃NH₃)₃Bi₂I₉

MAI = Methylammonium iodide, CH₃NH₃I

TGA = Thermogravimetric analysis

Acknowledgments

I would like to thank everyone who has helped me in completing this thesis from providing technical helps to valuable encouragements. Thanks to Prof. Banerjee, my advisor, for the patient guidance on professional work and the comfort advice on personal development. Thanks to all my group members, Yoon Myung, Zhengning Gao, Sriya Banerjee, Andreea Stoica, Howard Kim, and Peifu Cheng for their help in providing technique support. Thanks to all my friends, for encouraging and supporting me as always.

Thanks to Dr. Huafang Li at the Institute of Materials Science and Engineering for the microscopy facility and support. Thanks to Professor Singamaneni for Raman measurements. Thanks to Professor Sadtler for precursor preparations. Thanks to Professor Mishra and his group member Arashdeep and Dr. Sung for create crystal structures and theoretical supports. Support from Dr. D.C. Osborn at the XRD Facilities at University of Missouri St. Louis and Professor Flores at the optical microscope are graciously acknowledged. Thanks to my committee members, Prof. Singamaneni and Prof. Sadtler for taking the time to read the thesis and attend the defense.

Special thanks go to my advisor, Prof. Banerjee. I have learned a lot about professional engineering knowledge from him. More importantly, his guidance and supports on my personal career development will affect me forever in my career and life.

Xiao Chen

Washington University in St. Louis

August 2017

Dedicated to my parents.

Our family suffer a lot in the past year, but none of us give up with hope. I want to dedicate this thesis to my parents for their believing and supporting. Love you forever.

ABSTRACT OF THE THESIS

Single-step, Atmospheric Pressure Chemical Vapor Deposition for Methylammonium Bismuth

Iodide Thin Films

by

Xiao Chen

Master of Science in Materials Science Engineering

Washington University in St. Louis, 2017

Research Advisor: Professor Parag Banerjee

Lead halide perovskites ($\text{CH}_3\text{NH}_3\text{PbI}_3$ and its variants) are promising solar cell absorber materials. Though the reported power conversion efficiencies of lead halide perovskite solar cells (up to 21%) are competitive with commercial silicon solar cells, lead toxicity in these perovskites present a challenge to further scale-up and eventual commercialization. Recently, bismuth (Bi^{3+}) based organic halide perovskite has drawn attention as a substitution for lead-free perovskites, since it is a non-toxic 6p-block element, isoelectronic with Pb^{2+} . Methylammonium bismuth iodide ($(\text{CH}_3\text{NH}_3)_3\text{Bi}_2\text{I}_9$) is reported for its non-toxic constituents and favorable optical band gap, thus making it a promising light absorber material. However, manufacturing ready, scale-up processes have not been developed for this compound and this presents a significant roadblock in integrating low-cost, non-toxic Bi-based perovskites into modern solar cell devices.

Here, we report a single step, atmospheric pressure, chemical vapor deposition (CVD) process for $(\text{CH}_3\text{NH}_3)_3\text{Bi}_2\text{I}_9$. Atmospheric CVD addresses the need for rapid deposition across large area substrates, thus making the deposition of $(\text{CH}_3\text{NH}_3)_3\text{Bi}_2\text{I}_9$ thin films manufacturing-scalable. The precursors used are bismuth iodide (BiI_3) and methylammonium iodide ($\text{CH}_3\text{NH}_3\text{I}$) which are

sublimated and subsequently deposited inside a tube furnace reactor with a well-controlled temperature profile. Extensive characterization is conducted via grazing incidence X-ray diffraction, scanning electron microscopy, X-ray photoelectron spectroscopy, cyclic voltammetry, UV-vis spectroscopy and variable temperature Hall measurements. Structural and electronic stability of $(\text{CH}_3\text{NH}_3)_3\text{Bi}_2\text{I}_9$ films in ambient are measured and degradation mechanisms elucidated.

1 Introduction

1.1 Motivation

Photovoltaic solar cells are promising renewable power sources and are regarded as a viable future substitute for fossil-fuel-based electricity generation systems. Silicon-based and inorganic (e.g., cadmium telluride, CdTe) thin film photovoltaic solar panels are commercially available now and are readily available in the commodity market. However, the cost of production and the limitation of efficiency from material have driven people to search new photovoltaic materials. To reduce the dependence of fossil fuel and truly adopt an environmental friendly life style brought by photovoltaic solar cells, low cost, vacuum-free fabrication methods and non-toxic materials need to be used and this has led to the emergence of a new generation of thin film solar cells.

Perovskite based solar cells have emerged as one of the most promising of devices, where most of its layers are solution-processed. Lead halide perovskites ($\text{CH}_3\text{NH}_3\text{PbI}_3$ and its variants) is an interesting example, with reported power conversion efficiencies that have rapidly increased from¹ 3.8% in 2009, to an impressive² 22.1% in 2017. The fundamental material properties in lead halide perovskites that drive such progress are its high charge carrier mobilities³, high optical absorption coefficient,⁴ ideal and tunable bandgap⁵ and ultra-long carrier diffusion lengths up to a few microns.^{3,6,7}

Though the reported power conversion efficiencies of lead halide perovskite solar cells are competitive with commercial silicon solar cells, lead toxicity in these perovskites present a challenge to further scale-up and eventual commercialization. Recently, bismuth⁸ (Bi^{3+}) has drawn attention⁹ as a substituent to the A-site occupied by Pb^{2+} for 'lead-free' perovskites since it is a non-toxic 6p-block element that is isoelectronic¹⁰ with Pb^{2+} . Reports on promising optoelectronic and

photovoltaic properties of methylammonium bismuth iodide ($\text{MA}_3\text{Bi}_2\text{I}_9$, $(\text{CH}_3\text{NH}_3)_3\text{Bi}_2\text{I}_9$) with high absorption coefficient¹¹ and long term stability¹² have been published. However, $\text{MA}_3\text{Bi}_2\text{I}_9$ based solar cells suffer from low efficiency.¹³ This poor performance is suggested to originate from the solution deposition techniques that result in poor morphology and coverage of the perovskite films on substrate^{14,15}.

Therefore, in this thesis, we demonstrate a gas-phase deposition technique for $\text{MA}_3\text{Bi}_2\text{I}_9$ thin films using a low temperature (160 °C), atmospheric pressure chemical vapor deposition (APCVD) process. We obtain films with better process control over morphology, purity and coverage with the added advantage of rapid scale-up and integration with other solar manufacturing processes.

1.2 Atmospheric Pressure Chemical Vapor Deposition

Chemical vapor deposition (CVD) is used to deposit solid material onto a substrate. This involves the reaction or decomposition of one or more precursor gases in a chamber containing one or more heated substrates to be coated. The reactions occur on or near the hot substrate, resulting in the deposition of a thin film on the surface. The chemical by-products or unreacted gases are then eliminated from the reactor chamber via the exhaust system. A typical reaction process in CVD furnace is shown as Figure 1.1. First, mass transport of reactant and diluent gases in the bulk gas flow region from the reactor inlet to the deposition zone. Then, the gas phase reaction leading to form precursors and by-products. The mass transport of film precursors and reactants to growth surface, following with the adsorption of film precursors and reactants on the growth surface. After that, surface reaction of adatoms selectively occurring on the heated surface. Then the surface migration of film formers to the grows sites and nucleation. Finally, the desorption of by-products from surface reaction and mass transports in the bulk gas flow region away from the deposition zone¹⁶. CVD takes place under vacuum and high temperature to avoid inclusions in the film, or

creation of impurities from the side reaction of the precursor gases. Normally, the large diffusion coefficient at low pressure leading to a growth limited by the rate of surface reactions, but with a high purity and uniformity films.

Atmospheric-pressure chemical vapor deposition (APCVD) is a synthesis method where the substrate is exposed to one or more volatile precursors at atmospheric pressure, which react or decompose on the surface to produce a deposit. An APCVD reactor operates in the mass-transport regime so that wafer access become more important. APCVD is a good method for applying thin films to glass substrates¹⁷. The process has the advantage of being easily integrated into float-glass production lines with fast deposition rates¹⁸, simple process and lower reaction temperatures but may cause poor morphology and particle contamination without a sufficient flow of diluent¹⁹.

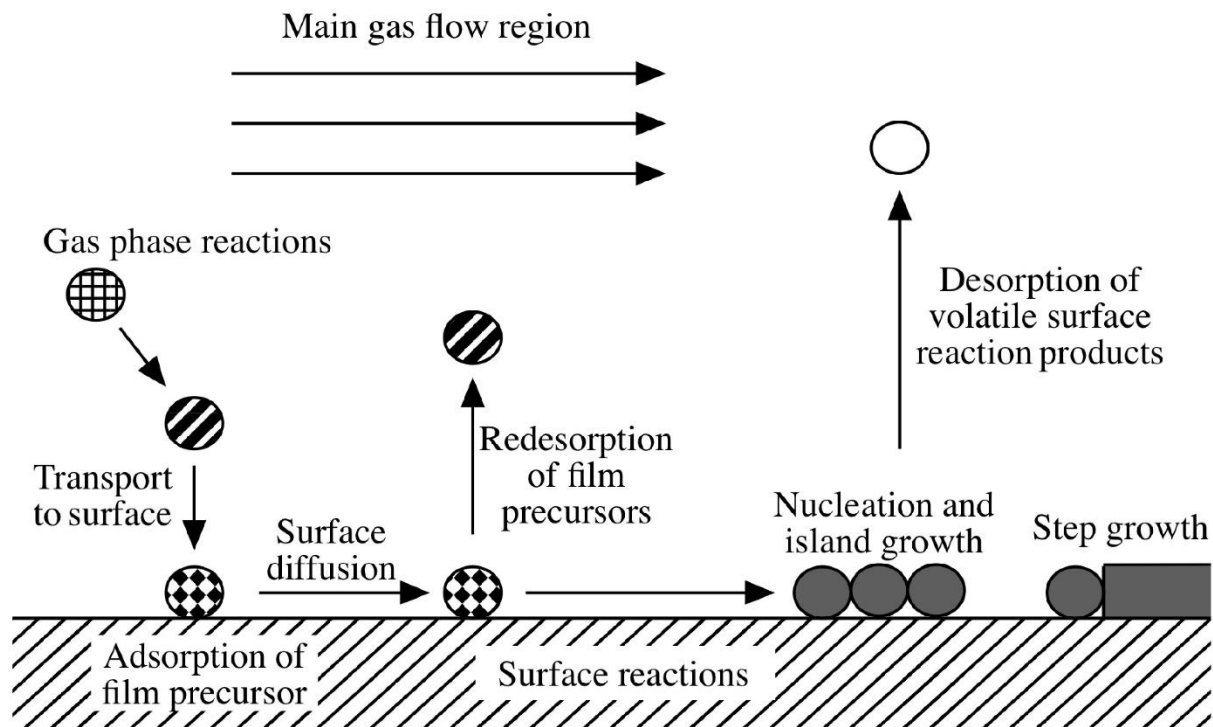
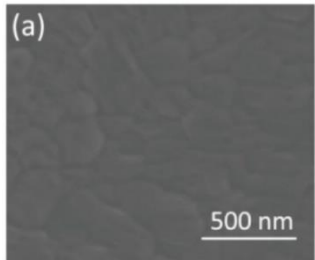
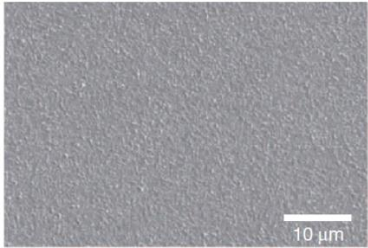
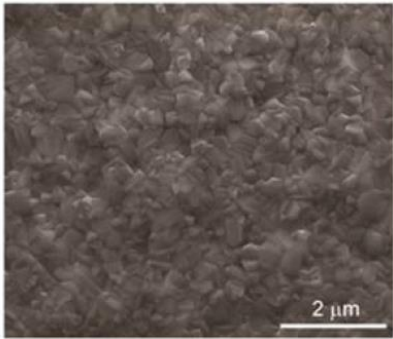


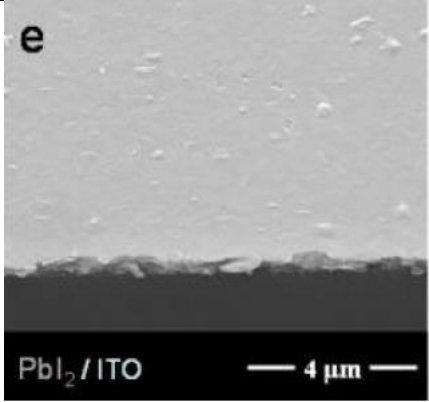
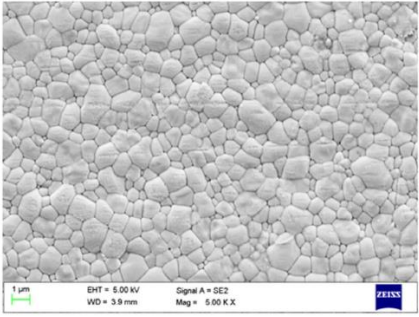
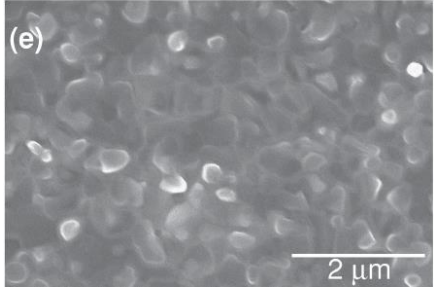
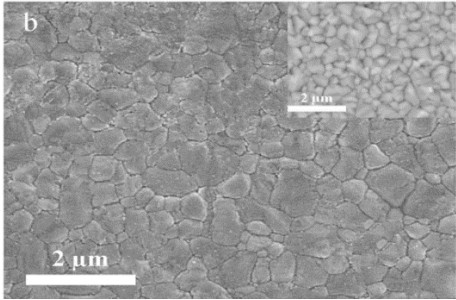
Figure 1.1 Schematic representation of the fundamental transport and reaction steps underlying CVD²⁰

1.3 Synthesis Routes for Organic-inorganic Halide Thin Films

Lead perovskites thin films have widely been prepared by dip/spin coating²¹⁻²³, gas-assisted spin coating processes^{14, 24-26} and gas involved annealing²⁷ after spin coating process. Vapor phase deposition methods have been reported for the formation of lead perovskite films as well. These include two step physical vapor deposition²⁸, single step physical vapor deposition²⁹, two step chemical vapor deposition^{30, 31} and single step chemical vapor deposition^{32, 33}. Details of these processes and the resultant film properties are provided in Table 1. However, there are no report of gas-phase processing of bismuth perovskite thin films. Furthermore, a detailed discussion of the mechanism of deposition of organic-inorganic halide thin films is missing in literature as well.

Table 1 different process and resultant film properties

Synthesis process	Perovskite	Precursors	SEM	Study (PCE%)
Dip/spin coating (By Ahn et al.) ²¹	$\text{CH}_3\text{NH}_3\text{PbI}_3$	$\text{CH}_3\text{NH}_3\text{I} + \text{PbI}_2$		Hole mobility $3.9 \times 10^{-3} \text{ cm}^2/(\text{V}\cdot\text{s})$; average PCE 18.3%
Gas-assisted spin coating (By Liu et al.) ¹⁴	$\text{CH}_3\text{NH}_3\text{PbI}_{3-x}\text{Cl}_x$	$\text{CH}_3\text{NH}_3\text{I} + \text{PbCl}_2$		PCE of over 15 %
Gas involved annealing (By Li et al.) ²⁷	$\text{CH}_3\text{NH}_3\text{PbI}_{3-x}\text{Cl}_x$	$\text{CH}_3\text{NH}_3\text{I} + \text{mixed PbCl}_2/\text{PbI}_2$		a top PCE of 16.8%,

<p>2-steps PVD (By Costa et al.)²⁸</p>	<p>No shown</p>	<p>PVD perovskite precursors PbCl₂, PbBr₂, and PbI₂.</p>		<p>Deposition perovskite precursors</p>
<p>1-step PVD (By Fan et al.)²⁹</p>	<p>CH₃NH₃PbI₃</p>	<p>CH₃NH₃PbI₃</p>		<p>A PCE of 10.9%;</p>
<p>2-steps CVD (By Chen et al.)³¹</p>	<p>CH₃NH₃PbI_{3-x}Cl_x</p>	<p>CH₃NH₃I+PbCl₂</p>		<p>A PCE of 15.4%; free of high-temperature fabrication</p>
<p>1-step CVD (By Tavakoli et al.)³³</p>	<p>CH₃NH₃PbI_{3-x}Cl_x</p>	<p>CH₃NH₃I+PbCl₂</p>		<p>A PCE of 11.1%</p>

Thus, the main objective of this thesis is to develop an APCVD process of lead-free perovskite films and formulate a deep understanding of the film forming mechanism, the structural properties and its inter-relationship with electrical and optical properties.

The structure of the thesis is as follows: Chapter 2 deals with experimental set up details. Chapter 3 provides details on the structural characterization of the APCVD process in lead-free perovskite films. Chapter 4 characterizes electrical and optical properties of films. Finally, chapter 5 discusses the degradation of film properties under ambient conditions. The contents of the following chapters are part of a manuscript entitled “Atmospheric Pressure Chemical Vapor Deposition of Methylammonium Bismuth Iodide Thin Films for Solar Cell Applications” which has been submitted to the Journal of Materials Chemistry - A.

2 Materials and Experiments

2.1 Precursors Preparations

2.1.1 Methylammonium iodide preparation & characterization

Methylammonium iodide (MAI, $\text{CH}_3\text{NH}_3\text{I}$) was synthesized using minor modifications to a previously published procedure³³. First, 25 mL of methylamine (33 wt% in ethanol, Sigma-Aldrich) was added to a 250 mL, three-neck flask maintained at a temperature lower than 7°C. 10 mL of hydroiodic acid (HI, 57 wt% in water, Sigma-Aldrich) was added dropwise to the flask at a speed of approximately 6 drops/10secs to MAI solution while the solution was stirred at 300 rpm. The white MAI precipitate was recovered from the solution using rotary evaporation at a pressure of 60 Torr with the flask in a water bath at 50 °C.

The collected MAI powder was dissolved in 10 ml absolute ethanol while stirring and sonicating for 10 minutes and then precipitated by adding 50-55 ml of diethyl ether to the solution. After filtration, the process was repeated 3 times, and finally a white powder was obtained and dried at 60 °C overnight under vacuum using a Schlenk line. The phase purity of the compound was confirmed by a Bruker D8 Advance powder X-ray diffractometer, as shown in Figure 2.1.

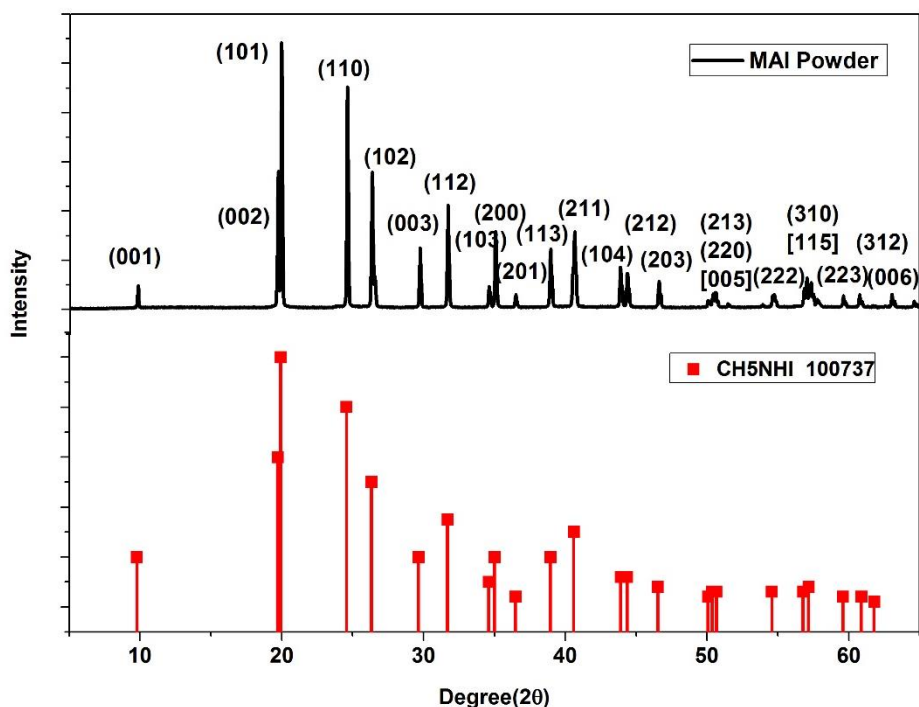


Figure 2.1 XRD of MAI powder (black) with corresponding JCPDS file # 100737 in red below.

2.1.2 Bismuth iodide preparation & characterization

BiI_3 powder was obtained from Aldrich, Inc. and used without further purification. For the synthesis of BiI_3 platelets, we controlled different deposition temperature by both the tube furnace temperature set system within a range from 200 °C to 300 °C and various types of substrates. The optical images are provided in Appendix A. The mass loss behavior of bismuth iodide (BiI_3) powders was generated through thermogravimetric analysis (TGA). TGA was performed using Q5000 IR (TA Instruments), heating at a steady heating rate (typically between 2.5 and 10 °C min^{-1}) under a constant 20 mL min^{-1} N_2 gas flow. The investigated temperature intervals were between a minimum of 25 °C to a maximum of 800 °C. Ceramic crucibles and approximately 5–15 mg of

sample material were employed for each measurement. The approach presented here is adapted from Dualeh et al.³⁴

2.2 Perovskite Synthesis via APCVD

The MAI powder prepared above and BiI₃ powder were used as precursors for APCVD. A quartz tube mounted on a single zone furnace (Compact Split Tube Furnace with 1" Tube-OTF-1200X-S, MTI Corporation.) was used for all APCVD studies. Silicon wafers (Test Grade, University Wafers Inc.) with a 100 nm thermal oxide layer, glass slides (48300-025, VWR) and pre-cut 5 mm x 5 mm high purity quartz substrates (MTI Corporation) were used as substrates. The silicon and glass substrates were cut to 1 cm x 2 cm size, ultrasonically cleaned in DI water, acetone (99.9% Aldrich) and ethanol (99.9% Aldrich) mixture for 10 minutes, washed by IPA and DI water, dried in compressed air, cleaned in UV Ozone (Ossila E511) for 10 minutes, and then immediately placed in the quartz tube at 23 cm away from the upstream. The temperature of APCVD furnace was measured by customized program attached with N-type thermocouple and a MAX 31856 single chip microcomputer. The details were attached in Appendix A.

Initially, 50 mg of MAI and 60 mg of BiI₃ were used as sources and placed at 2.5 cm and 13 cm from the upstream end of the quartz tube in alumina boat crucibles. First, the quartz tube was purged with 280 standard cubic centimeters per minute (sccm) flow of ultra-high purity Ar gas (UHP 300, Airgas) for 10 minutes. The temperature in the quartz tube was then raised at a rate of 3.4 °C / minute until the temperature at the center of the tube reached 230 °C. The furnace was maintained at this temperature for various times of 15, 30, 45, 60, 90, 180, 240, 360 and 480 minutes of deposition. After deposition, the furnace was naturally allowed to cool down to ambient temperature. This usually took 3 hours. The detailed discussion on synthesis process is presented in chapter 3.

2.3 Film Characterization

Film morphology was characterized by a JEOL JSM-7001 LVF Field Emission SEM under an accelerating voltage of 10 kV. X-ray diffraction (2 θ scans) of deposited MA₃Bi₂I₉ films were obtained by Rigaku IV X-ray diffractometer using the Cu K α X-ray source ($\lambda = 1.5405 \text{ \AA}$) within a diffraction angle (2 θ) from 5° to 60°. X-ray photoelectron spectroscopy (XPS) was measured using the PHI Versa Probe II spectrometer (Physical Electronics) with a photon energy of 1486.6 eV (Al K α). A UV–vis spectrophotometer (UV-1800, Shimadzu) was used to measure optical transmittance of the MA₃Bi₂I₉ films on glass substrates.

The electrochemical analysis was performed with a standard three-electrode cell using the cyclic voltammetry (CV) mode in a Biologic potentiostat (SP-200, Bio-Logic SAS) with a scan rate of 20 mV/s. This approach presented here is adapted from Myung et al³⁵. MA₃Bi₂I₉ films was used as the working electrode, a Pt foil acted as the counter electrode, and Ag/0.01 M AgNO₃ + 0.1 M tetrabutylammonium hexafluorophosphate (TBAPF₆) (98%, Aldrich) acetonitrile (99.9%, Sigma-Aldrich) as the reference electrode (BAS Inc.). The conduction band (CB) energy was calculated from the onset of reduction potential (E_{red}) values, assuming the energy level of ferrocene/ferrocenium (Fc/Fc⁺) to be -4.8 eV below the vacuum level. The formal potential of Fc/Fc⁺ was measured in 0.001 M Ferrocene (99%, Sigma-Aldrich) in 15 mL 0.1 M TBAPF₆ acetonitrile to be 0.075 V against a Ag/Ag⁺ reference electrode. Therefore, from equation (2.1)

$$E_{\text{CB}} (E_{\text{LUMO}}) = - (E_{\text{red}} + 4.725) \text{ eV}, \quad (2.1)$$

where the onset potential values(E_{red}) are relative to the Ag/Ag⁺ reference electrode. The valence band (VB) energy, $E_{\text{VB}} (E_{\text{HOMO}})$ was calculated based on the band gap value determined from UV–vis spectra, $E_{\text{VB}} (E_{\text{HOMO}}) = E_{\text{CB}} - E_{\text{g}}$ (indirect). MA₃Bi₂I₉ films deposited on glass slides were immersed in a solution of 0.1 M TBAPF₆, acetonitrile for conducting these tests.

All electronic transport property measurements were carried out in a commercial probe station (Janis ST500-1-2CX) with Cu–Be probe tips having 50 μm tip-diameter. A Keithley 2400 source meter was used for resistivity measurements on $\text{MA}_3\text{Bi}_2\text{I}_9$ films deposited on 5 mm \times 5 mm high-purity quartz substrates (MTI Corp). Van der Pauw structures were created by first sputtering 50 nm Pt on the four corners of the quartz substrates prior to $\text{MA}_3\text{Bi}_2\text{I}_9$ deposition. After $\text{MA}_3\text{Bi}_2\text{I}_9$ deposition, indium dots were attached to these four corners and served as the contact electrodes for the four probe tips. Corresponding Hall measurements were done by placing an Fe-Nd ring-magnet around the sample. The magnetic-field strength at the center of the ring magnet was 2135 G. The pressure in the chamber was maintained at or below 1×10^{-4} Torr.

3 Bismuth Perovskites Synthesis via APCVD

3.1 APCVD process

As described in chapter 2, the schematic of the experimental set-up is shown in Figure 3.1a, while a picture of the furnace after successful $\text{MA}_3\text{Bi}_2\text{I}_9$ deposition is shown in Figure 3.1b. The deposition is marked by the characteristic orange color of the $\text{MA}_3\text{Bi}_2\text{I}_9$ film on the downstream side.⁸

The key aspect of an APCVD process lies in the precise placement of the MAI and BiI_3 sources along the length of the quartz furnace reactor. This allows us to co-sublimate both the sources together. Figure 3.1c shows the temperature profile of the furnace along the length of the CVD quartz tube. This calibration measurement was done prior to the deposition by sliding a thermocouple probe inserted inside the quartz tube with Ar flowing at the rate of 280 sccm. The temperature varies from 199 °C from the upstream end (labeled as 2.5 cm on the x-axis) and peaks to the desired temperature set-point of the furnace (230 °C) at the center of the tube (13 cm from the upstream end). The temperature then drops off on the downstream side to 160 °C, 23 cm from the upstream end. Details on profiling temperature inside the furnace is provided in Appendix A.

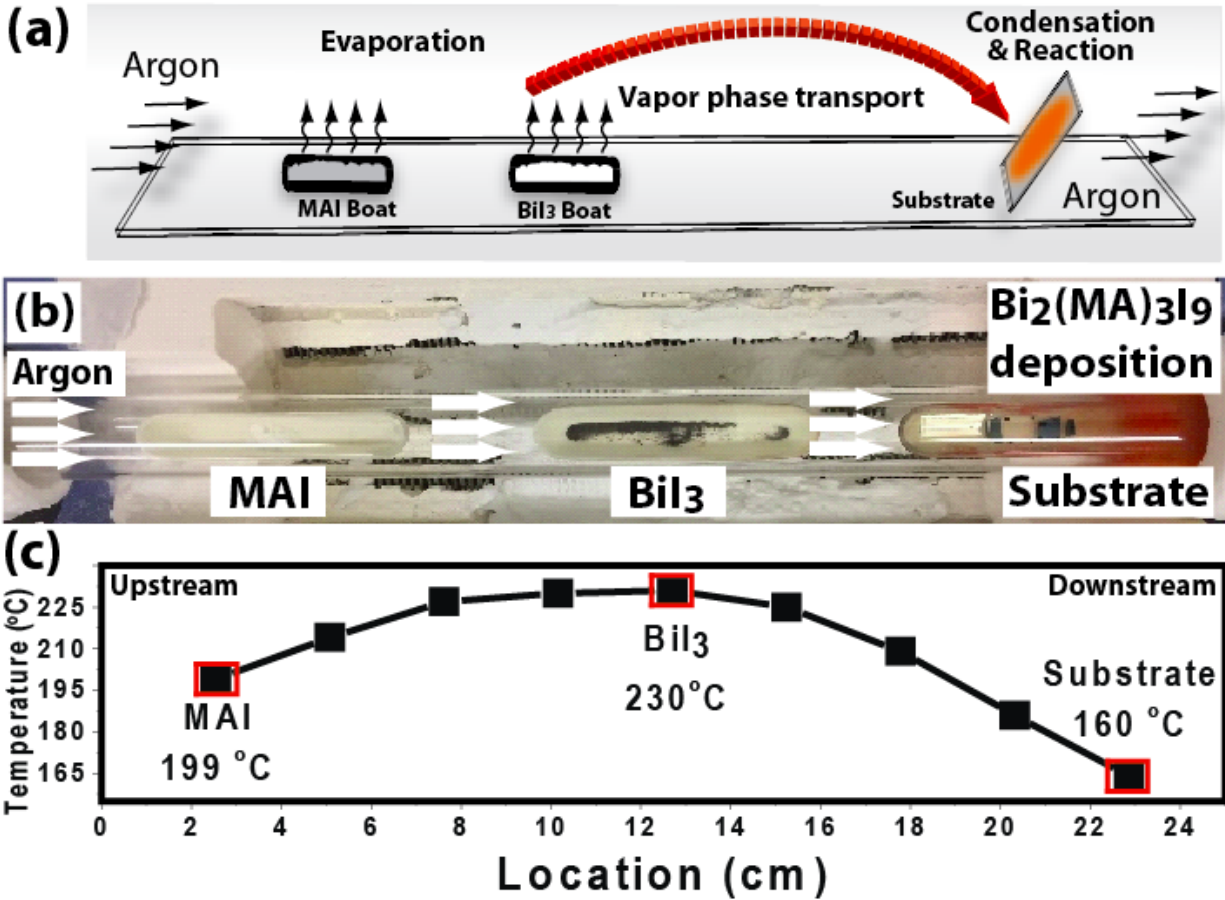


Figure 3.1 (a) Schematic of APCVD for $\text{MA}_3\text{Bi}_2\text{I}_9$ thin films, (b) Image of MAI and BiI_3 boats inside the tube furnace and (c), temperature profile of the tube furnace showing the MAI and BiI_3 sublimation temperatures and $\text{MA}_3\text{Bi}_2\text{I}_9$ film deposition temperature.

MAI is kept in the upstream side of the quartz reactor where the temperature is 199 °C. We note that MAI has a melting point of 270 °C. The BiI_3 is kept in the middle of the quartz reactor where the temperature is 230 °C. BiI_3 has a melting point³⁶ of 402 °C but is known to sublime as well. Thus, the Ar flow causes the simultaneous transport of MAI and BiI_3 vapor to the cooler zone in the downstream region. Condensation and reaction of the MAI and BiI_3 vapors take place to produce the $\text{MA}_3\text{Bi}_2\text{I}_9$ film at around 23 cm from the upstream side, where the temperature is maintained at 160 °C.

3.2 Vapor Pressure Calculations

The detailed mass loss measurements and vapor pressure calculations of the two precursors MAI and BiI₃ and compared their partial pressures at the points of sublimation and deposition. The data for MAI is directly obtained from Dualeh et al.,³⁴. The data for BiI₃ is obtained from our experiments, as described below.

The Clausius-Clapeyron relation relates the vapor pressure p and the temperature T of a solid with its enthalpy of sublimation ΔH_{sub} , where R is the gas constant ($8.314\text{J}\cdot\text{K}^{-1}\cdot\text{mol}^{-1}$) according to equation (3.1)³⁷

$$\frac{d \ln p}{dt} = \frac{\Delta H_{sub}}{RT^2} \quad (3.1)$$

The first derivative of the TGA heat curve gives a direct measure of the instantaneous rate of mass loss m_{sub} at temperature T ,

$$\frac{dm}{dt} = \frac{\Delta m}{\Delta t} = m_{sub} \quad (3.2)$$

In equilibrium conditions, the rates of vapor condensation and evaporation are assumed to be equal. Hence the rate of mass loss by sublimation m_{sub} can be related to the vapor pressure by equation (3.3) according to Langmuir³⁸ where A is the exposed sublimation surface area (here we take the area calculated from the TGA sample pan during the measurement) and M_w is the molecular mass of the material.

$$p = \frac{1}{A} \left(\frac{2\pi RT}{M_w} \right)^{\frac{1}{2}} m_{sub} \quad (3.3)$$

Integrating equation (3.1) yields equation (3.4), which allows the determination of ΔH_{sub} , and sublimation temperature T_{sub} from the slope and x-intercept of the plot of $\ln p$ vs. $1/T$, respectively:

$$\ln p = -\frac{\Delta H_{sub}}{R} \left(\frac{1}{T} - \frac{1}{T_{sub}} \right) \quad (3.4)$$

Based on this approach, Figure 3.2a shows the weight loss of BiI₃ powder as a function of heating rate. The corresponding rate of weight loss (dm/dt) is shown in Figure 3.2b. Therefore, using equation (3.3) it is possible to calculate p , the vapor pressure for BiI₃. This is plotted as a semi-log plot as a function of $1/T$ in Figure 3.2c. As a result, the vapor pressure of BiI₃ can be calculated from equation (3.4). This is shown in Figure 3.2d. As stated previously, the vapor pressure of MAI is obtained from Dualeh et al.³⁴

Next, using the known temperature profile of the furnace, it is possible to calculate the partial vapor pressures of MAI, BiI₃ at the point of sublimation and at the point of condensation (i.e. at the substrate). The vapor pressure as a function of temperature is provided in Table 2. The enthalpy of sublimation (ΔH_{sub}) and sublimation temperature (T_{sub}) of BiI₃ obtained from equation (3.4) are found to be 128 ± 2 kJ/mol and 316 ± 2 (°C), respectively as shown in Table 3.

Table 2 The partial pressures obtained from thermogravimetric analysis of MAI and BiI₃ powders

	Precursor compound	Process	Temp (°C)	Partial pressure (atm)	MAI: BiI ₃ ratio	
					Sublimation	Deposition
1	MAI	Sublimation	199 °C	0.0846	4.7:1	
2	BiI ₃	Sublimation	230 °C	0.0180		
3	MAI	Deposition	160 °C	0.01133		87:1
4	BiI ₃	Deposition	160 °C	0.00013		

Table 3 The enthalpy of sublimation (ΔH_{sub}) and sublimation temperature (T_{sub}) are shown for both the precursors

Precursor	ΔH_{sub} (kJ/mol)	T_{sub} (°C)
BiI ₃ (this work)	128 ± 2	316 ± 2
MAI (Dualeh et al. ³⁴)	105 ± 5	247 ± 26

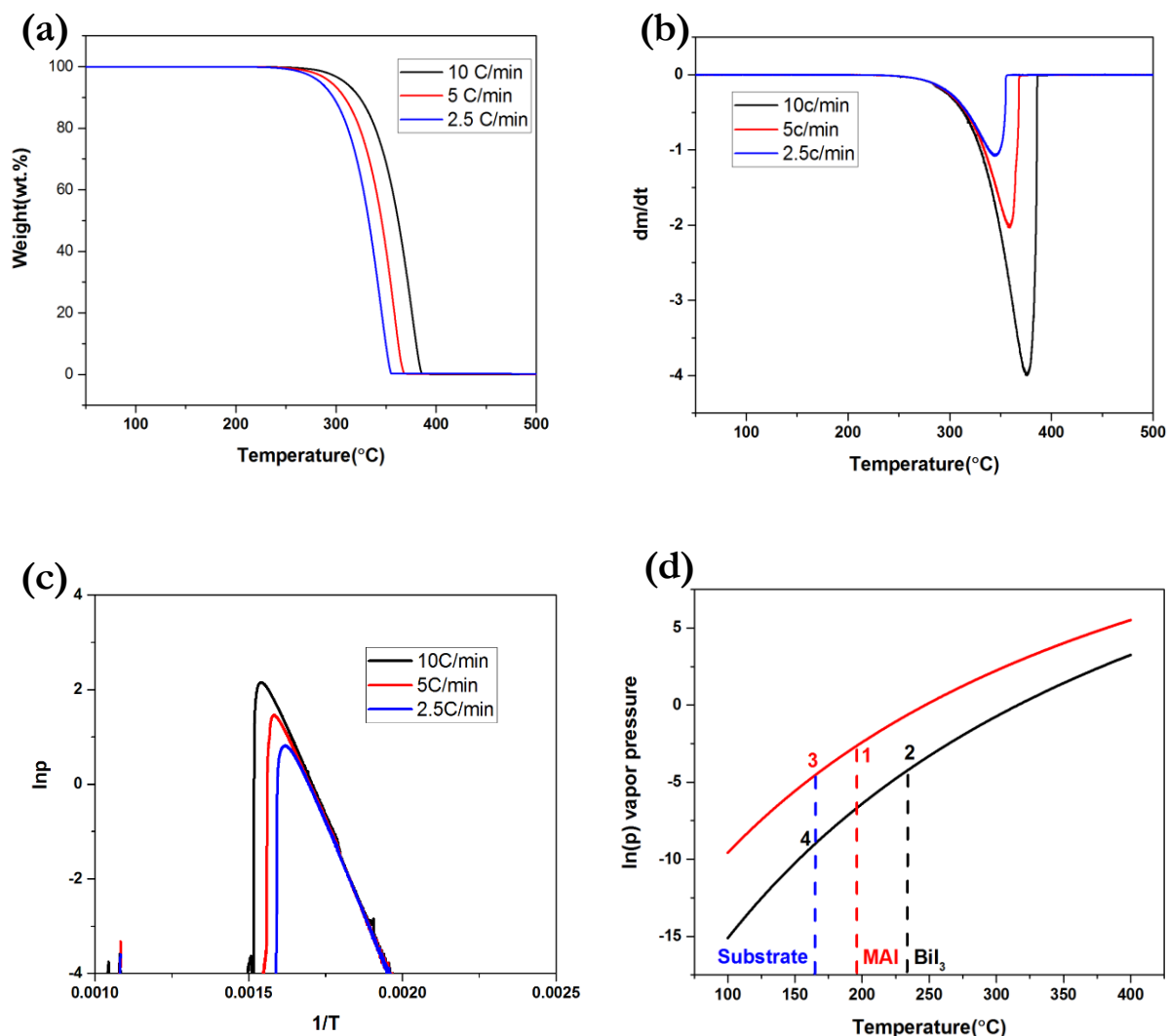


Figure 3.2 : (a) TGA heating curves of the BiI₃ precursor and (b) corresponding 1st derivatives measured at different heating rates of BiI₃ precursor; (c) calculated ln p vis 1/t of BiI₃ precursor. (d) vapor pressure of BiI₃ (black) and MAI (red) precursors as a function of temperature. The dotted vertical lines indicate the position where the MAI crucible (199 °C), BiI₃ crucible (230 °C) and substrate (160 °C) are placed in the horizontal tube furnace.

It can be seen that the MAI vapor pressure is 4.7x of vapor pressure of BiI₃ as both the precursors sublime inside the furnace, but at different temperatures (199 °C for MAI and 230 °C for BiI₃). Since the molecules travel downstream to the cooler zone, condensation occurs. At the

point of deposition, the temperature on the substrate = 160 °C. Here, MAI remains more volatile and the ratio of the equilibrium vapor pressure of MAI: BiI₃ = 87. Further, the driving force for condensation is proportional to $\ln (p_{\text{sublimation}}/p_{\text{condensation}})$ which for MAI = 2.01 and for BiI₃ = 4.93. This implies that the BiI₃ should readily condense on the substrate, nucleate and grow. On the other hand, we find that the condensation of MAI followed by a solid-state reaction with BiI₃ to form MA₃Bi₂I₉ is the kinetically rate-determining step. This conclusion is in line with the observations via SEM, XRD and XPS, as discussed in following sections.

3.3 Mechanism of Film Deposition and Growth

From the previous vapor pressure calculations, one can conclude that BiI₃ should easily condense and nucleate on the substrate first. The APCVD perovskite film process is actually a two-step process, with BiI₃ deposit first and then MAI followed by a solid-state reaction with BiI₃ to form MA₃Bi₂I₉ in the kinetically rate-determining step. Understanding BiI₃ deposition requirements is necessary to setting up experiments for APCVD process. Herein, we consider BiI₃ vapor deposition first, and optimize the deposition temperature to 230 °C, and Silicon wafers with 100 nm thick thermal oxidation layer as substrates of BiI₃ deposition and further APCVD process. The detailed visual images are provided in Appendix B.

High-magnification SEM images are shown in Figure 3.3. Mechanistic aspects of the deposition process can be garnered from this sequence of images. First, Figure 3.3a, b and c (i.e., for deposition times 15, 30 and 45 minutes) show isolated hexagonal crystals growing in size from 0.5 μm for 15 minutes, to 1.0 μm for 45 minutes of deposition. The crystal shape is characteristic of BiI₃³⁹ and has been independently confirmed by through Raman (see Figure 3.4) and XRD measurements, as will be shown below. Thus, in the initial part of the deposition scheme, isolated BiI₃ crystals 0.5 – 1.0 μm in diameter are deposited on the substrate surface.

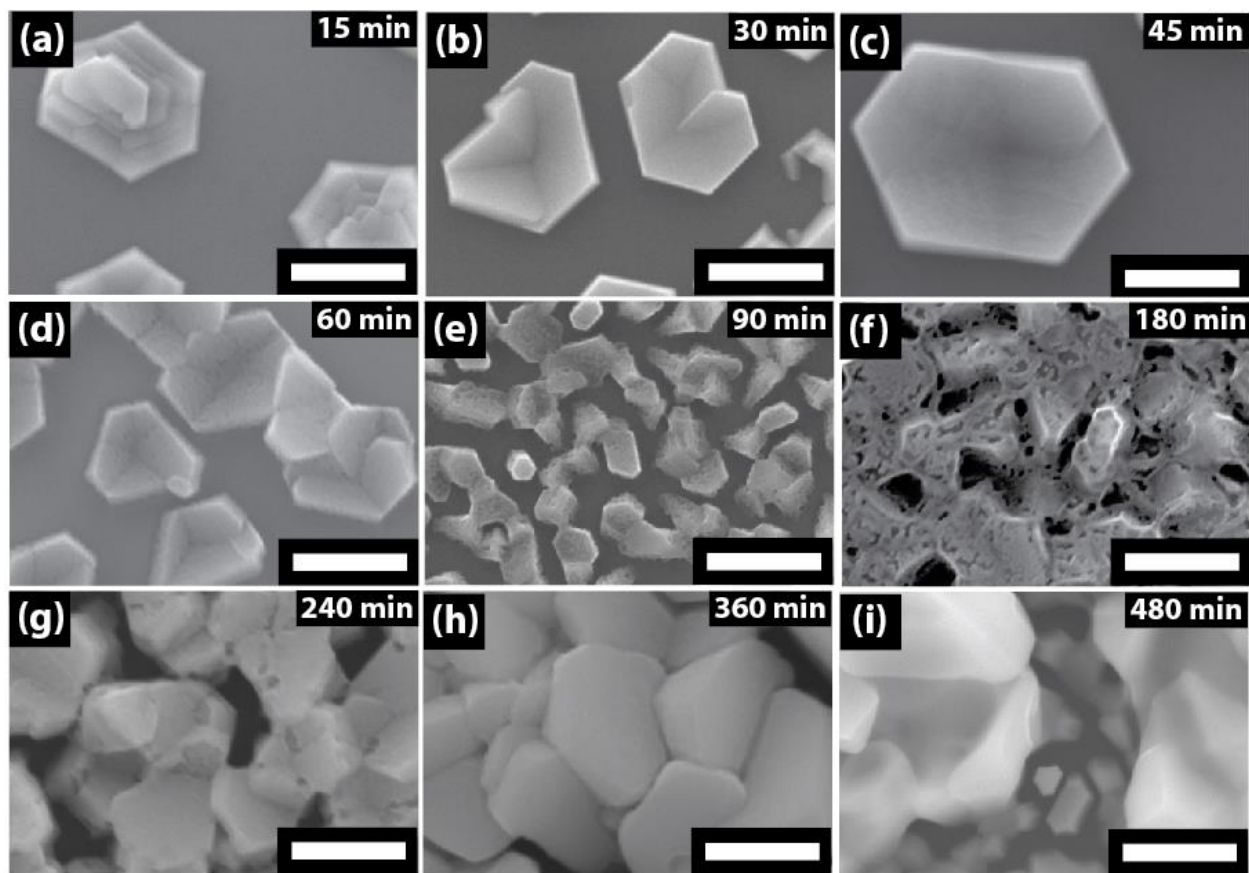
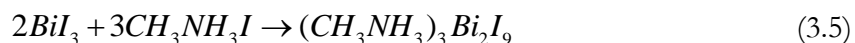


Figure 3.3 SEM images of APCVD films for varying times of deposition. Scale bar = 500 nm.

The BiI_3 crystals show signs of MAI incorporation starting at 60 minutes (Figure 3.3d). While the crystal shapes remain intact, the surface of the crystal shows marked roughness. For 90 minutes (Figure 3.3e), the deposited structure becomes interconnected. The interconnected structure shows signs of growth for 180 minutes (Figure 3.3f), while the surface structure is rough and full of pinholes. In this region, the phase transformation from BiI_3 to $(\text{CH}_3\text{NH}_3)_3\text{Bi}_2\text{I}_9$ starts to happen as follows equation (3.5):



The surface structure further changes for the 240-minute sample (Figure 3.3g), where well-crystallized $\text{MA}_3\text{Bi}_2\text{I}_9$ grains are visible, though evidence of MAI incorporation can still be seen at

the grain boundaries. For the 360-minute sample (Figure 3.3h), the $\text{MA}_3\text{Bi}_2\text{I}_9$ polycrystalline grains are well developed, indicating complete incorporation of MAI. However, there are intergranular gaps observed, and such morphology is not ideal for thin-film photovoltaic application. Finally, for the 480-minute sample (Figure 3.3i), we see secondary nucleation of grains in between larger polycrystalline grains.

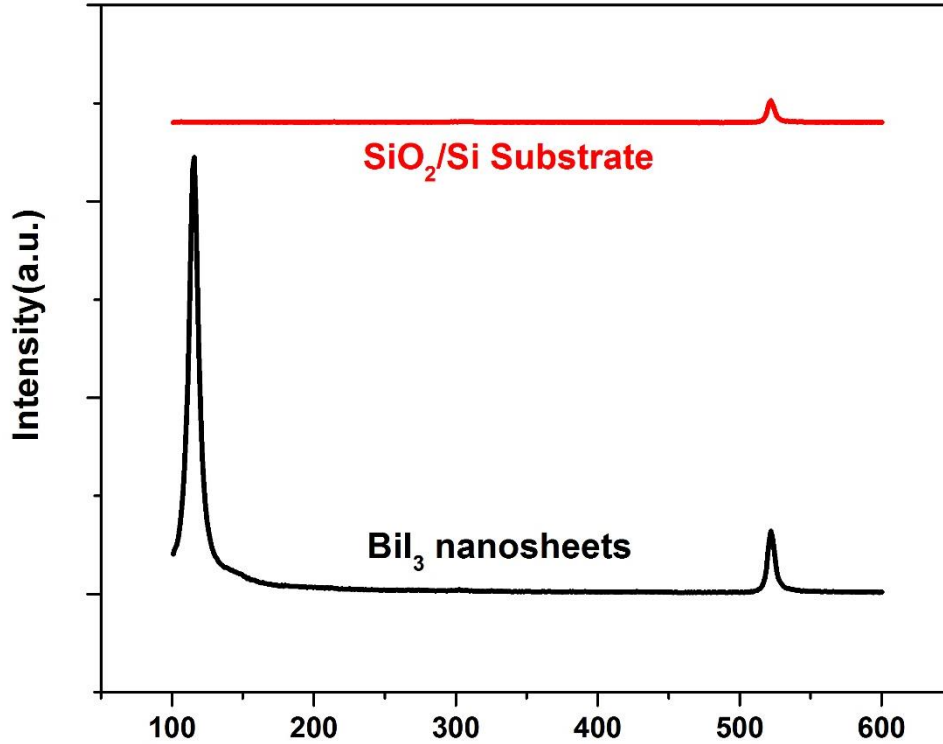


Figure 3.4 Raman spectroscopy of BiI_3 nanosheets. The Raman signal from SiO_2/Si substrate on which the BiI_3 were deposited are as a comparison.

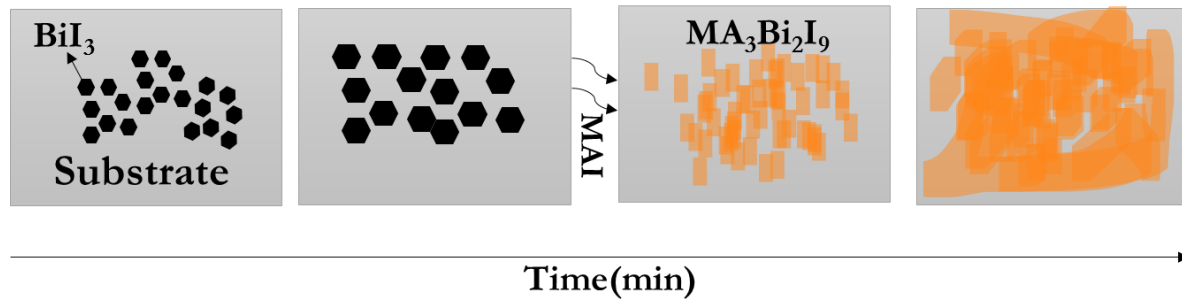


Figure 3.5 Schematic of deposition process mechanism in APCVD

As for solution processed^{10, 40-42} MA₃Bi₂I₉ films, usually the chemical reaction happened as long as precursors met, and need further 30-120 minutes for post reaction annealing at 100-150 °C. Compared to solution processed MA₃Bi₂I₉ films, APCVD process in this thesis needs a longer time to detect the phase transformation, which may due to the difference of driven force or the restrictions of chamber size in this particular case.

As shown in Figure 3.5, a schematic of the APCVD deposition process mechanism, BiI₃ and Ar carrier gas mass transport to the deposition zone, BiI₃ then condense on the substrate, nucleate and grow. Then MAI condense and incorporate at surface, followed by a solid-state reaction with BiI₃ to form MA₃Bi₂I₉ and nucleate.

Figure 3.6 shows the color of the films on glass substrates as a function of the deposition time. Initially, for short times (< 60 minutes), there is hardly any deposition observed. After 90 minutes of reaction, a visible orange color is seen on the glass substrate. We note that there is a stronger color close to the upstream side of the sample, indicating that the deposition is determined by the Ar flow. For films ≥ 180 minutes, a continuous film is observed on the glass substrate. The orange color is characteristic of MA₃Bi₂I₉⁸ and, as will be shown later, is representative of its optical bandgap.

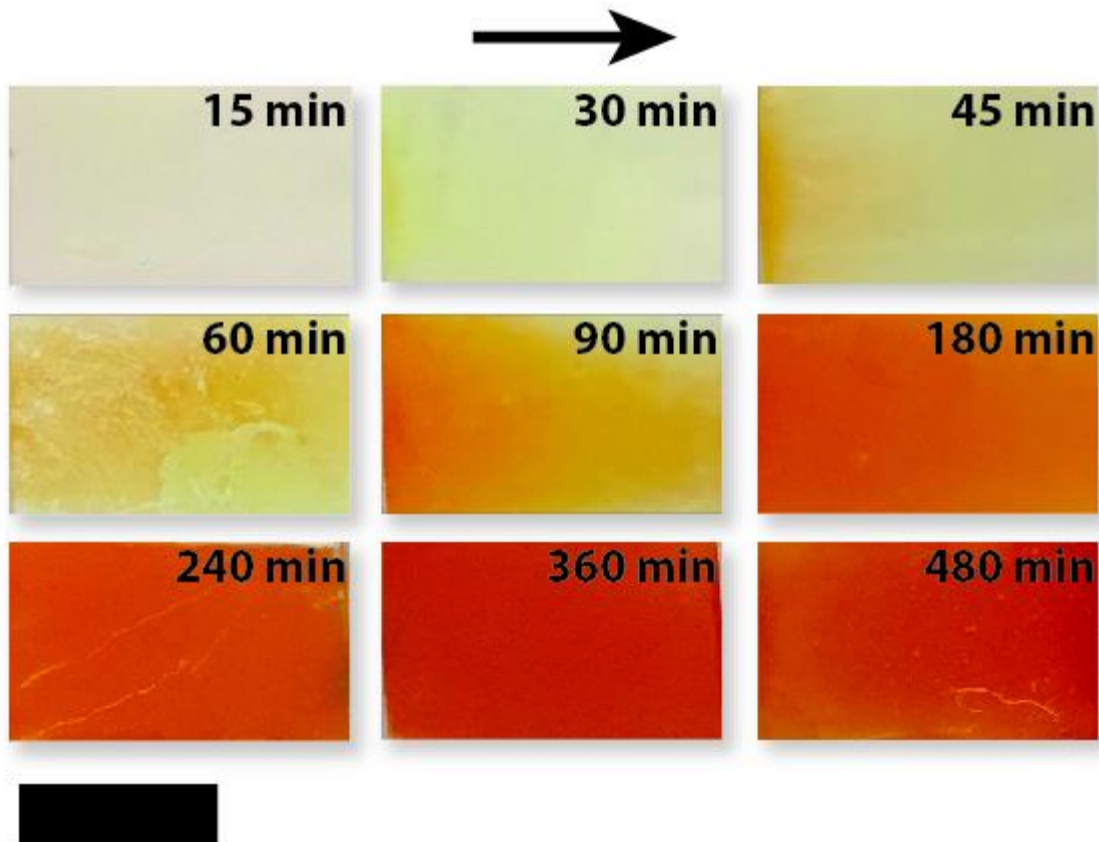


Figure 3.6 Optical images of APCVD MA₃Bi₂I₉ films on glass substrate for varying times of deposition. Arrow represents direction of Ar flow in the furnace. Scale bar = 1 cm.

We have used the secondary growth of the MA₃Bi₂I₉ crystals in the intergranular regions to grow a dense, compact and polycrystalline film. From Figure 3.3(h), a SEM image of the 360-minute sample is shown. The intergranular regions are clearly observed and, as indicated before, are sites for secondary nucleation after 480 minutes of deposition. Repeating the process twice (labeled henceforth as, 360 minute (2×)), can eliminate these gaps and produce a film with dense morphology. This is shown in Figure 3.7 with a side view to determined thickness for further characterizations and a top view of dense morphology. While such an approach may see long deposition times, its need is dictated primarily by the limited mass loading of the MAI and BiI₃ precursors in our sublimation crucibles. Larger furnace reactors may easily overcome such hardware

limitations and yield dense films in a single-process run. The ‘twice-deposited’ films were subsequently used to conduct all the optical and electrical measurements.

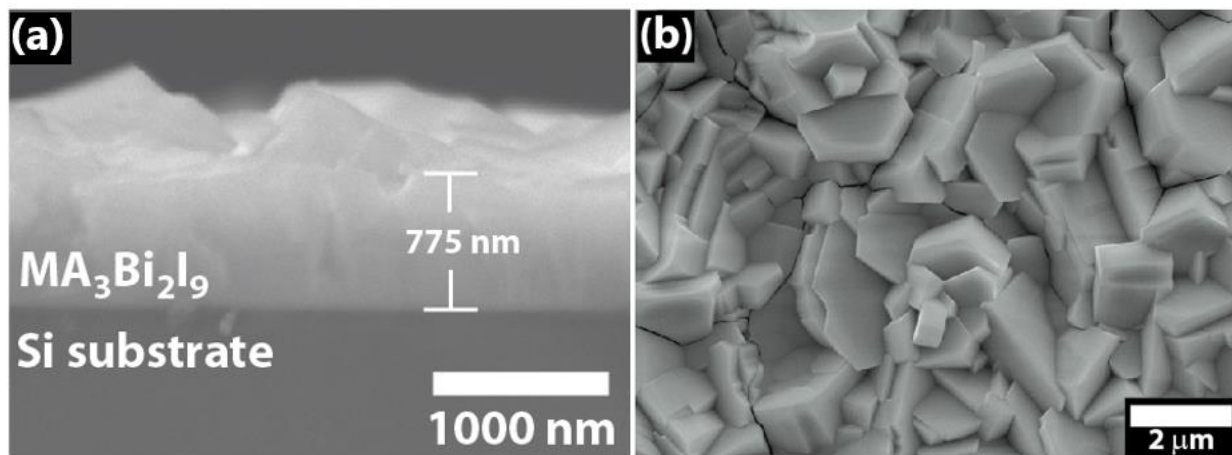


Figure 3.7 (a) Side view of MA₃Bi₂I₉ film deposited twice for 360 minutes shows a thickness of 775 nm. **(b)** A repeat of MA₃Bi₂I₉ film deposited for 360 minutes, eliminates these gaps and produces a dense, polycrystalline film. All optical and electrical measurements were performed on the 360 minutes (2×) sample.

3.4 Structure of MA₃Bi₂I₉

XRD data of all the MA₃Bi₂I₉ samples deposited for various times are shown in Figure 3.8a. For times between 15 – 60 minutes, clear diffraction peaks of BiI₃ with symbol ‘○’ can be seen. The peak at $2\theta = 52.9^\circ$ can be indexed⁴³ to BiI₃ (0012). The other peaks represent MAI, marked by the symbol ‘●’, (JCPDS ref no. 000-10-0737). There is also a peak for MA₃Bi₂I₉ at $2\theta = 44.5^\circ$, but it is weak and gradually starts to increase in intensity only after 45 minutes of deposition. Here, we note

that there are no JCPDS files available for $\text{MA}_3\text{Bi}_2\text{I}_9$ and we use the patterns generated by Abulikemu et al. to index our peaks⁴⁴.

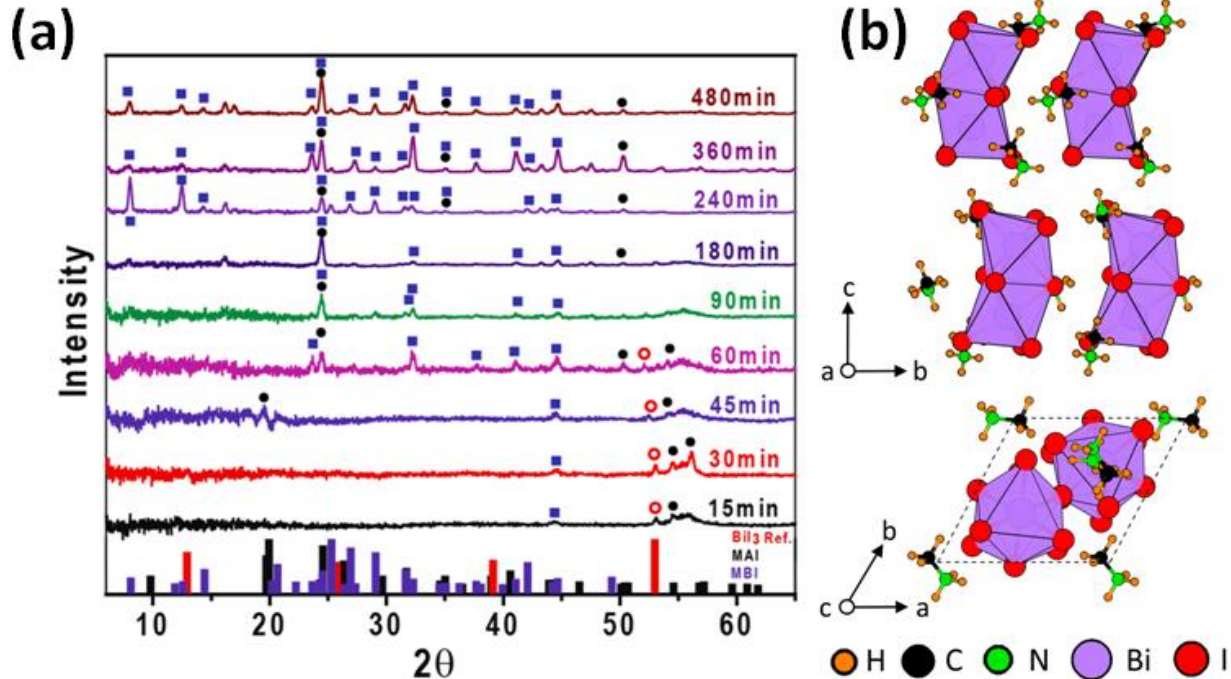


Figure 3.8 (a) XRD of the $\text{MA}_3\text{Bi}_2\text{I}_9$ films as a function of deposition time. Single crystal BiI_3 reference is obtained from Boopathy et al., and is indexed with symbol ‘○’. MAI reference is obtained from JCPDS ref no. 000-10-0737 and is indexed with symbol ‘●’. $\text{MA}_3\text{Bi}_2\text{I}_9$ reference is obtained from Abulikemu et al., and is indexed with symbol ‘■’. (b) Crystal structure of $\text{MA}_3\text{Bi}_2\text{I}_9$ after relaxation along (100) (top) and (001) (bottom) crystallographic directions.

After 60 minutes’ of deposition, the presence of $\text{MA}_3\text{Bi}_2\text{I}_9$ is detectable through XRD. The $\text{MA}_3\text{Bi}_2\text{I}_9$ phase is denoted by the ‘■’ symbol. The primary peaks are at $2\theta = 24.48^\circ$, 32.30° and 44.62° corresponding to (006), (025) and (220), respectively⁴⁴. These results are in line with SEM data which show the MAI incorporation begins at 60 minutes of deposition time. A texturing effect is observed for the 180-minute sample where the primary peak at $2\theta = 24.48^\circ$ is observed. However, given that there are multiple peaks all corresponding to $\text{MA}_3\text{Bi}_2\text{I}_9$, the peak at $2\theta = 24.48^\circ$ is most likely from the $\text{MA}_3\text{Bi}_2\text{I}_9$ phase. Here we note that a transient texturing effect could be indicative of

a topotactic transformation between MAI and MA₃Bi₂I₉. Beyond the 180-minute sample, the XRD patterns are characteristically polycrystalline with multiple peaks, all assignable to MA₃Bi₂I₉. These data are in-line with SEM data since polycrystallinity is clearly shown in SEM images for 240-, 360- and 480-minute samples.

Next, we compare the lattice parameters from our XRD results to the crystal structure data obtained from first-principles DFT calculations. MA₃Bi₂I₉ exhibits hexagonal crystal symmetry at room temperature with *P6₃/mmc* space group.⁴⁵⁻⁴⁷ The methylammonium cation (CH₃NH₃⁺ (MA⁺)) shows no preferential ordering in the hexagonal phase.⁴⁵

The MA₃Bi₂I₉ structure can be thought of as a derivative of the perovskite (*ABX₃*) structure. In both cases the *B*-site cation (Bi in case of MA₃Bi₂I₉) is octahedrally coordinated by *X*-site anions (I in case of MA₃Bi₂I₉). However, as compared to the ideal perovskite structure, only 2/3 of the total octahedral sites are occupied by the Bi cation in *A₃Bi₂I₉* compounds.⁴⁸ Additionally, as opposed to the corner-connected octahedral network of *BX₆* octahedra in perovskites, MA₃Bi₂I₉ forms a layered structure consisting of isolated Bi₂I₉³⁻ bioctahedra. These bioctahedra are formed by two face-shared BiI₆ octahedra, which share three I anions (Figure 3.8b).

Figure 3.9 shows the XPS fine spectra of the 15-, 180- and 480-minute MA₃Bi₂I₉ films whereas the full survey spectra of these samples are provided in Appendix C. In Figure 3.9a, the C 1s fine spectrum is shown. For the 15-minute sample, the primary peak is at 284.5 eV corresponding to the C-C bond related to adventitious carbon. There is a slight shoulder detected at 282.6 eV, which is related to the C-N bond⁴⁹ originating from MAI. The C-N bond increases in strength for the 180-minute sample and dominates the C 1s signal for the 480-minute sample. These data suggest that MAI incorporation in the BiI₃ is a slower process than the BiI₃ condensation, nucleation and

growth process. This conclusion is in line with earlier observations made from vapor pressure calculations in Table 2 as well as SEM images in Figure 3.3.

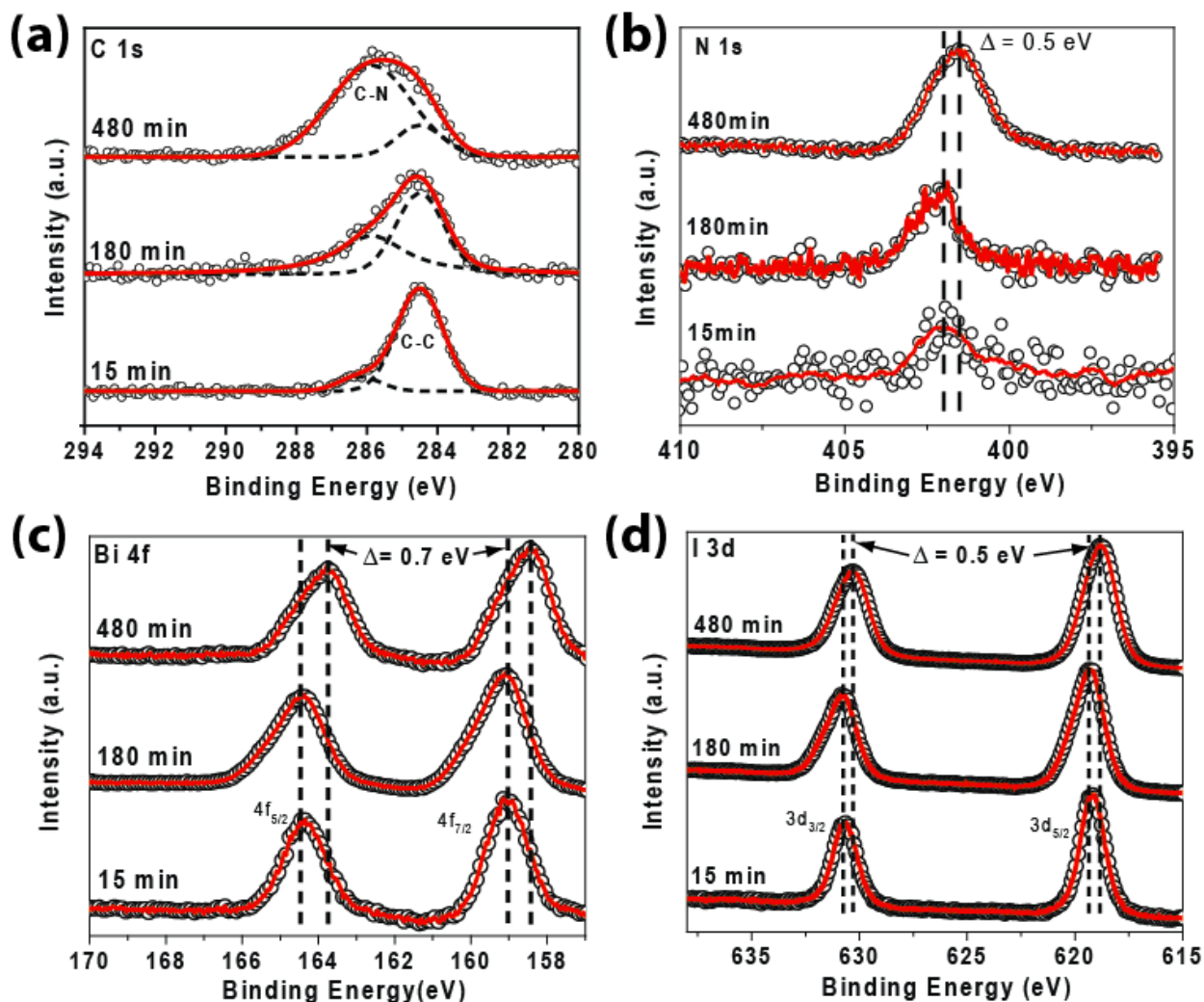


Figure 3.9 XPS fine spectra obtained from 15, 180 and 480 minute MA₃Bi₂I₉ thin films showing (a) C 1s, (b) N 1s, (c) Bi 4f and, (d) I 3d. The carbon 1s peak has been deconvoluted into two peaks related to adventitious carbon (284.5 eV) and C-N from the methylammonium group.

N 1s, Bi 4f and I 3d XPS fine spectra are provided in Figure 3.9b, c and d, respectively, and the peak positions are shown in Table 4. For the N 1s spectra, the 15-minute sample shows a weak signal but progressively grows stronger for the 180- and 480-minute samples indicating MA⁺

incorporation. The N 1s peak position shifts to lower binding energy from 402.0 eV to 401.5 eV. The Bi 4f and I 3d peaks are strong even at 15 minutes and indicate the presence of BiI₃. MA⁺ incorporation produces a shift to lower binding energy of 0.7 eV and 0.5 eV in the Bi 4f and I 3d peaks, respectively. The peak-shifts indicate electron transfer to the N, Bi and I during the transformation of BiI₃ to MA₃Bi₂I₉.

Table 4 XPS peak positions of N1s, Bi 4f_{7/2} and I 3d_{5/2} in the MA₃Bi₂I₉ films deposited for 15, 180 and 480 minutes.

Sample	Binding Energy (eV)		
	N 1s	Bi 4f _{7/2}	I 3d _{5/2}
480 min	401.5	158.4	618.8
180 min	402.0	159.0	619.2
15 min	402.0	159.1	619.3

3.5 Conclusions

The MA₃Bi₂I₉ film has been successfully synthesized through an APCVD process. The film is deposited using co-sublimation of methyl ammonium iodide (kept at 199 °C) and BiI₃ (kept at 230 °C) as precursors. The temperature of deposition is 160 °C. BiI₃ readily condense on the substrate, nucleate and grow; the condensation of MAI followed by a solid-state reaction with BiI₃ to form MA₃Bi₂I₉, which is the kinetically rate-determining step. The morphology and composition of the films is characterized via SEM, XRD and XPS to confirm the hypothesis from vapor pressure calculations. Well-developed crystals (over 1 μm grain size) are obtained after 360 minutes of deposition. Repeating the process twice leads to dense, high quality polycrystalline films.

4 Optical & Electrical Characterization

4.1 Optical Characterization

Figure 4.1a shows the UV-vis absorption spectra of MA₃Bi₂I₉ at wavelengths 400 nm and 1000 nm. The absorption onset of MA₃Bi₂I₉ was observed at approximately 600 nm. The presence of a peak at 511 nm before the onset of continuous absorption is attributed to excitons.⁵⁰⁻⁵³ This exciton peak has also been observed for single crystals of MA₃Bi₂I₉ from temperatures between 78 K to 301 K and it starts to broaden as the temperature increases.⁵¹

The detailed bandgap of MA₃Bi₂I₉ films was calculated⁵⁴ by the Tauc equation:

$$\alpha h\nu = \beta(h\nu - E_g)^n, \quad (4.1)$$

where α is the absorption coefficient, $h\nu$ is the photon energy, β is a constant, and E_g is the bandgap; a linear fit is used to extract the bandgap. Assuming the lowest energy optical transition in MA₃Bi₂I₉ is indirect), $n=1/2$ is used in the evaluation. Figure 4.1b shows the Tauc plot, and the extrapolated bandgap is 2.08 eV. The value of the MA₃Bi₂I₉ bandgap is in line with those reported by Lyu et al.¹⁰

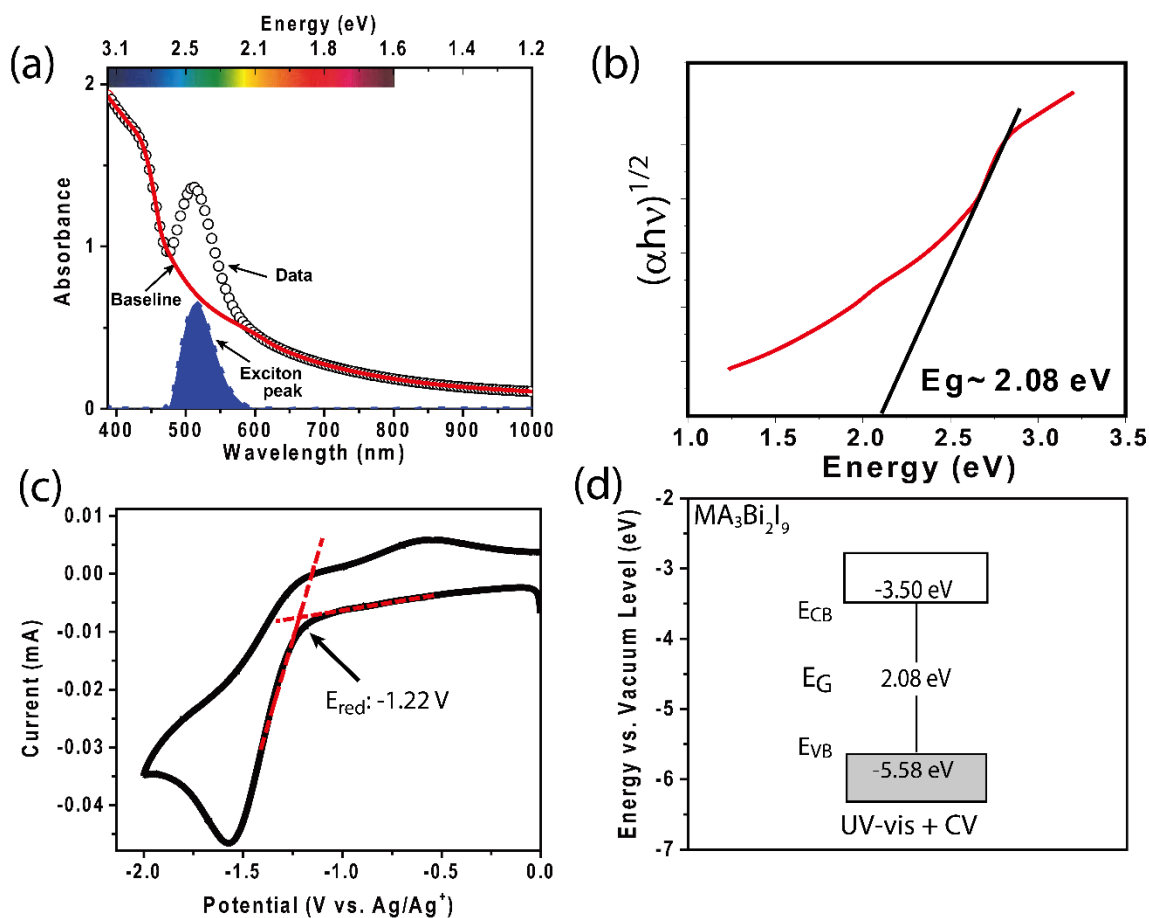


Figure 4.1 (a) UV- vis spectra of MA₃Bi₂I₉ film. (b) Exciton peak is extracted and a Tauc plot of the baseline is used to measure the indirect bandgap ~ 2.08 eV (c) Cyclic voltammetry curve (vs. Ag/Ag⁺ electrode) for MA₃Bi₂I₉ (d) Band edge information from experimental (UV-vis + CV)

To extract the experimental band edge positions of the MA₃Bi₂I₉, CV measurements are shown in Figure 4.1c. MA₃Bi₂I₉ has the reduction peak edge at, $E_{red} = -1.22$ V. Referring to equation (2.1), the MA₃Bi₂I₉ conduction band edge position is therefore calculated as, $E_{CB} = -3.505$ eV with respect to vacuum. Using the bandgap obtained from UV-vis, the valence band edge position is

calculated as $E_{VB} = -5.58$ eV. The data from UV-vis and CV measurements are summarized in Figure 4.1d.

4.2 Electrical Characterization

For the $\text{MA}_3\text{Bi}_2\text{I}_9$ film deposited twice (360 minute ($2\times$)) on the quartz substrate, conductivity was measured using a van der Pauw four-point configuration. The conductivity is $9.7 \text{ S}\cdot\text{cm}^{-1}$ (i.e., resistivity $0.103 \text{ }\Omega\cdot\text{cm}$) at room temperature for a film with a thickness of 775 nm (see Figure 3.7(a) for thickness measurement using cross-section SEM image). The detailed result is shown in Table 5 along with comparison of electrical data from other reports.^{10,41} This conductivity is 1168x better than the reported conductivity ($0.0083 \text{ S}\cdot\text{cm}^{-1}$) of a solution-processed,¹⁰ 500 nm $\text{MA}_3\text{Bi}_2\text{I}_9$ film highlighting the importance of the type of synthesis in determining film properties.

Room temperature Hall measurement was performed to determine conductivity type, carrier mobility and concentration of the $\text{MA}_3\text{Bi}_2\text{I}_9$ film. According to the measurements, the Hall coefficient is negative, which indicates the carriers to be *n*-type for the CVD $\text{MA}_3\text{Bi}_2\text{I}_9$ film. This result is in contrast to the solution processed $\text{MA}_3\text{Bi}_2\text{I}_9$ films, which show *p*-type conductivity^{10,41} and may indicate ionic impurities in the solution processed film, which could mask the intrinsic electronic conductivity of the $\text{MA}_3\text{Bi}_2\text{I}_9$ film. Further, the calculated carrier concentration of the CVD $\text{MA}_3\text{Bi}_2\text{I}_9$ film is $3.36 \times 10^{18} \text{ cm}^{-3}$, which is 2 orders higher in magnitude than solution-based, undoped $\text{MA}_3\text{Bi}_2\text{I}_9$ films.^{10,41} Finally, the mobility was estimated to be $18 \text{ cm}^2/\text{V}\cdot\text{s}$. This is higher compared to the mobility reported by Lyu et al.,¹⁰ of $1 \text{ cm}^2/\text{V}\cdot\text{s}$ and Vigneshwaran et al.,⁴¹ of $2.28 \text{ cm}^2/\text{V}\cdot\text{s}$.

Additionally, we have performed variable temperature hall measurements on these films. However, our data across different samples was not consistent. These data are provided in Appendix D. Briefly, there is a transition region around 150K for carrier densities and mobilities for

both samples, indicating a possible phase transition point near 150K, which in line with Kamminga⁵⁵ et al. report.

Table 5 Comparison of Hall measurement data of MA₃Bi₂I₉ films deposited using various synthesis techniques.

Synthesis process	Thickness (nm)	Conductivity (S·cm ⁻¹)	Mobility (cm ² /V·s)	Carrier density (cm ⁻³)
APCVD 360 minutes (2×) (this work)	775	9.7	18.0	<i>n</i> -type 3.36 × 10 ¹⁸
Solution processed (Lyu et al., ^[16])	500	0.0083	1.0	<i>p</i> -type 10 ¹⁶
Solution processed, Sulphur doped (Vigneshwaran et al., ^[46])	unknown	839	2.28	<i>p</i> -type 2.3 × 10 ²¹

4.3 Conclusion

Optical bandgap is measured to be 2.08 eV from UV-VIS spectra and cyclic voltammetry, implies it is a promising light absorber, along with an onset characteristic exciton effect. Room temperature Hall measurements on 775 nm thick MA₃Bi₂I₉ films indicate them to be *n*-type with a carrier concentration of $3.36 \times 10^{18} \text{ cm}^{-3}$ and a Hall mobility of $18 \text{ cm}^2/\text{V}\cdot\text{s}$; values superior to solution processed, undoped films, which implies the difference of synthesis process result in optimal electrical properties.

5 Film Stability

5.1 Material Characterization

It has been reported that the $\text{MA}_3\text{Bi}_2\text{I}_9$ is stable in ambient, thus presenting a significant advantage over other organic halide perovskite candidates.¹² However, in our work we find that $\text{MA}_3\text{Bi}_2\text{I}_9$ film exposed to ambient (room temperature, 45% humidity and 1 atm) undergoes changes to its composition and degradation to its optical and electrical properties. In Figure 5.1a, we detect a loss of N in the $\text{MA}_3\text{Bi}_2\text{I}_9$ film exposed to the ambient in just 5 days. The absence of N has been observed by Li et al.,⁵⁶ for degraded Pb-based perovskite films as well. Figure 5.1b shows XPS fine spectra of I $3d_{3/2}$ and $3d_{5/2}$ for fresh films and for films exposed 5 and 14 days to the ambient. Shoulders appear for the I $3d_{3/2}$ and $3d_{5/2}$ peaks on the higher binding energy side, indicating the oxidation⁵⁷ of I in the film due to its interaction with ambient oxygen. Further, in Figure 5.1c, we provide the XPS 1s fine spectra of O in the $\text{MA}_3\text{Bi}_2\text{I}_9$ film. The fresh sample shows O 1s peak at 532.5 eV corresponding to hydroxyl groups adsorbed on the surface of the $(\text{MA})_3\text{Bi}_2\text{I}_9$. After 5 days, a shoulder emerges on the lower binding energy (530.4 eV) side which indicates lattice bonded oxygen with Bi which progressively grows stronger after 14 days.⁵⁸ This means the characteristic O peak associated with surface adsorbed hydroxyl groups with an additional shoulder corresponding to Bi-O bond formation after 5 days and growing stronger after 14 days of exposure to the ambient. In Figure 5.1d, The Bi $4f_{7/2}$ shifts from 159 eV to 159.8 eV after 5 days. This is a result of the conversion of Bi from an iodine octahedral environment to Bi_2O_3 . After 14 days the Bi $4f_{7/2}$ returns to 158.9 eV. This is because of the mixing of the oxide and iodide states of Bi to form BiOI .⁵⁹ Further, a distinct but broad shoulder appears at 161.7 eV (marked by arrows). As in the case of O 1s fine spectra, this peak is characteristic of a hydrated surface.⁵⁷

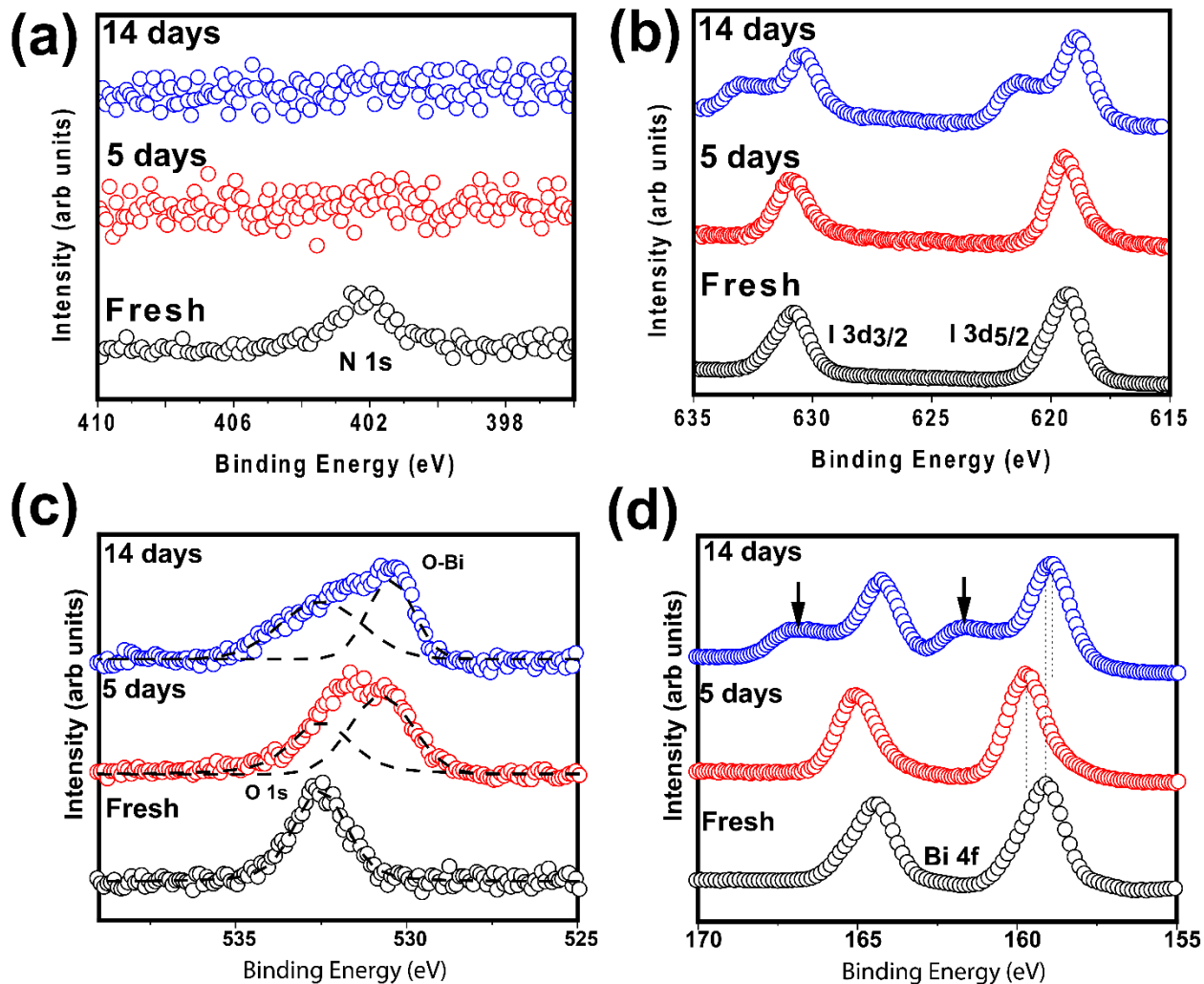


Figure 5.1 (a) XPS fine spectra of N 1s shows absence of N after just 5 days exposure in ambient. (b) XPS fine spectra of I 3d for fresh, after 5 (no change) and 14 days in ambient. (c) XPS fine spectra of O 1s for fresh and after 5, 14 days in ambient. (d) XPS fine spectra of Bi 4f for fresh (black) and after 5 (red) and 14 days (blue) in ambient.

5.2 Optical & Electrical Characterizations

The compositional changes in the $\text{MA}_3\text{Bi}_2\text{I}_9$ are accompanied by corresponding changes to optical and electrical properties as well. Figure 5.2a shows the UV-vis absorption spectra of the $\text{MA}_3\text{Bi}_2\text{I}_9$ film exposed to ambient over a period of 5 days. The characteristic 510 nm exciton peak disappears on day 5. Correspondingly, the film changes color from bright orange to a pale shade of yellow, as insert in Figure 5.2a. In Figure 5.2b, the excitonic intensity at 510 nm (black, left axis) and the 4-wire resistivity (red, right axis) are plotted as a function of time over a five day period. A bi-exponential model involving two time constants is used to fit the increase in resistivity over time. Two time constants, $\tau_1 = 0.1$ day and $\tau_2 = 1.7$ days are obtained with a model fit that has an adjusted $r^2 \sim 0.99$.

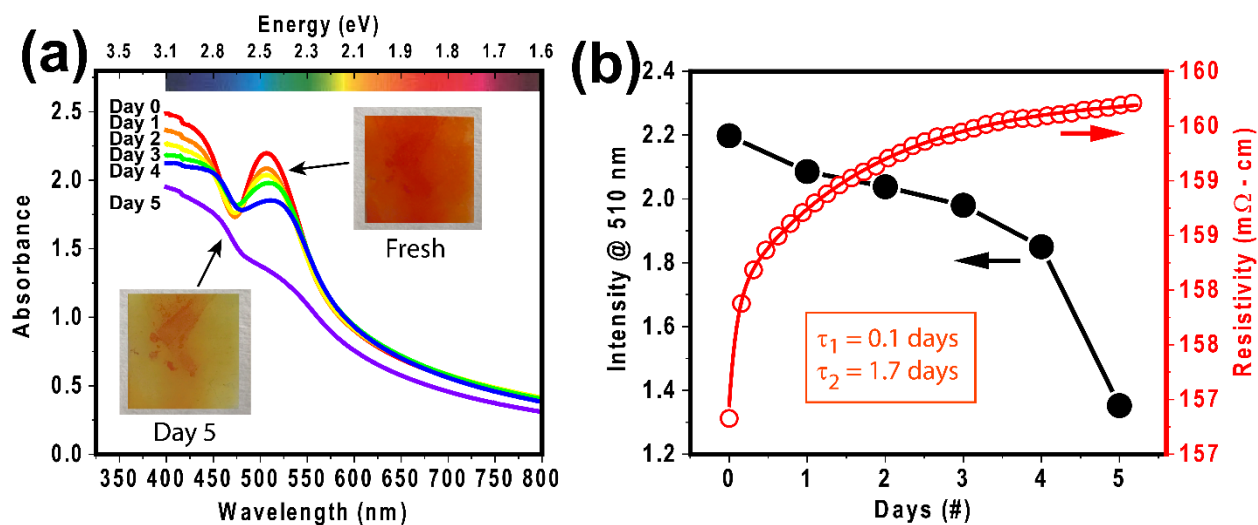


Figure 5.2 (a) UV-vis spectra from day 0 (fresh) to day '5' shows a gradual decay of the excitonic peak while insets show actual film fading color, and (b) Change in exciton peak intensity (black, left axis) and electrical resistivity (red, right axis) as a function of number of days exposed to ambient. The increase in resistivity follows a bi-exponential decay with time constants 0.1 and 1.7 days.

5.3 Conclusion

The XPS analysis along with the bi-exponential decay of resistance suggests two decay mechanisms might be operative in degrading the $\text{MA}_3\text{Bi}_2\text{I}_9$ films. First, the time constant $\tau_1 = 0.1$ day could indicate surface oxidation of $\text{MA}_3\text{Bi}_2\text{I}_9$ where the Bi may be oxidized to Bi_2O_3 . In line with this assumption, it can be seen that the characteristic exciton peak intensity only slightly degrades in the initial period. This is because the surface Bi_2O_3 layer may provide temporary protection¹² from further attack by ambient O_2 , keeping the excitonic modes active in the bulk. On the other hand, $\tau_2 = 1.7$ days indicates the slower diffusion limited oxidation of the bulk $\text{MA}_3\text{Bi}_2\text{I}_9$ and as the film gets oxidized after day 4, the rate of degradation of the exciton peak intensity increases significantly. The $\text{MA}_3\text{Bi}_2\text{I}_9$ films oxidize under ambient conditions in a matter of ~ 5 days and in the process, 1) N is lost, 2) excitonic peaks are quenched and, 3) resistivity increases with a bi-exponential decay with time constants related to a fast surface oxidation mechanism, followed by a slower oxidation of the bulk film.

6 Conclusion

We have demonstrated an atmospheric pressure chemical vapor deposition process for the deposition of MA₃Bi₂I₉ perovskite film. The film is deposited using co-sublimation of methyl ammonium iodide (kept at 199 °C) and BiI₃ (kept at 230 °C) as precursors. The temperature of deposition is 160 °C. BiI₃ readily condense on the substrate, nucleate and grow; the condensation of MAI followed by a solid-state reaction with BiI₃ to form MA₃Bi₂I₉, which is the kinetically rate-determining step. The morphology and composition of the films is characterized via SEM, XRD and XPS to confirm the hypothesis from vapor pressure calculations. Well-developed crystals are obtained after 360 minutes of deposition. Repeating the process twice leads to dense, high quality polycrystalline films for further studies.

Optical bandgap is measured to be between 2.08 eV from UV-VIS spectra and cyclic voltammetry, implies it is a promising light absorber, along with an onset characteristic exciton effect. Room temperature Hall measurements on 775 nm thick MA₃Bi₂I₉ films indicate them to be *n*-type with a carrier concentration of $3.36 \times 10^{18} \text{ cm}^{-3}$ and a Hall mobility of $18 \text{ cm}^2/\text{V}\cdot\text{s}$; values superior to solution processed, undoped films, which implies the difference of synthesis process result in optimal electrical properties.

The MA₃Bi₂I₉ films oxidize under ambient conditions in a matter of ~5 days and in the process, 1) N is lost, 2) excitonic peaks are quenched and, 3) resistivity increases with a bi-exponential decay with time constants related to a fast surface oxidation mechanism, followed by a slower oxidation of the bulk film.

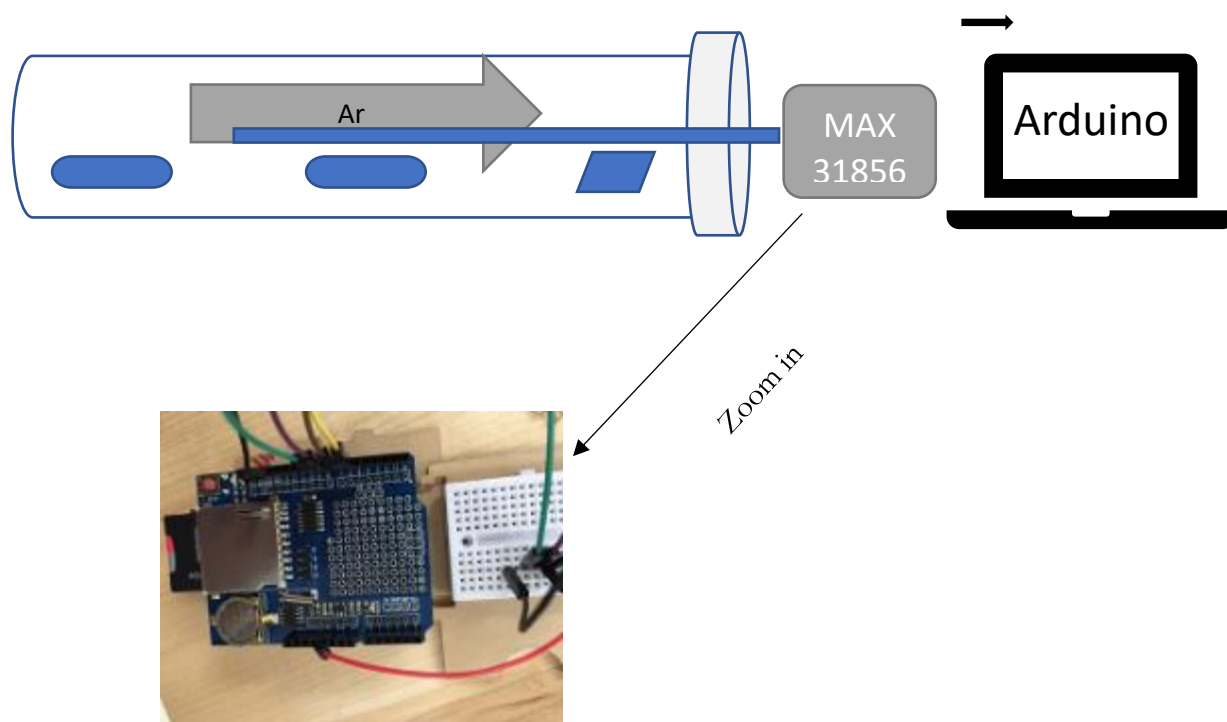
7 Future Work

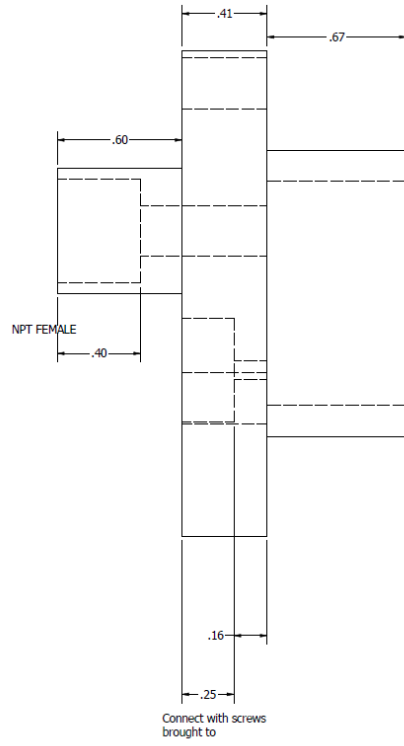
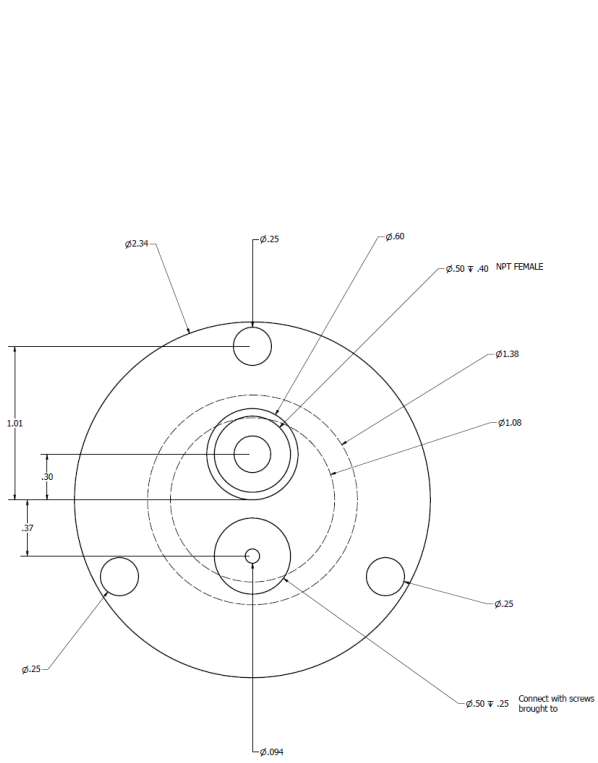
Future effort can be focus on *in-situ* electrical characterizations MA₃Bi₂I₉ films during APCVD process. In this thesis, all the material characterizations were generated on films synthesized after a certain time period in APCVD furnace. Since we already know the bare film stability in ambient conditions, it is possible that the films have explored the oxidation before the *ex-situ* material characterizations. Besides, the *in-situ* electrical characterizations could also provide a hint on continuous changes happened inside APCVD furnace.

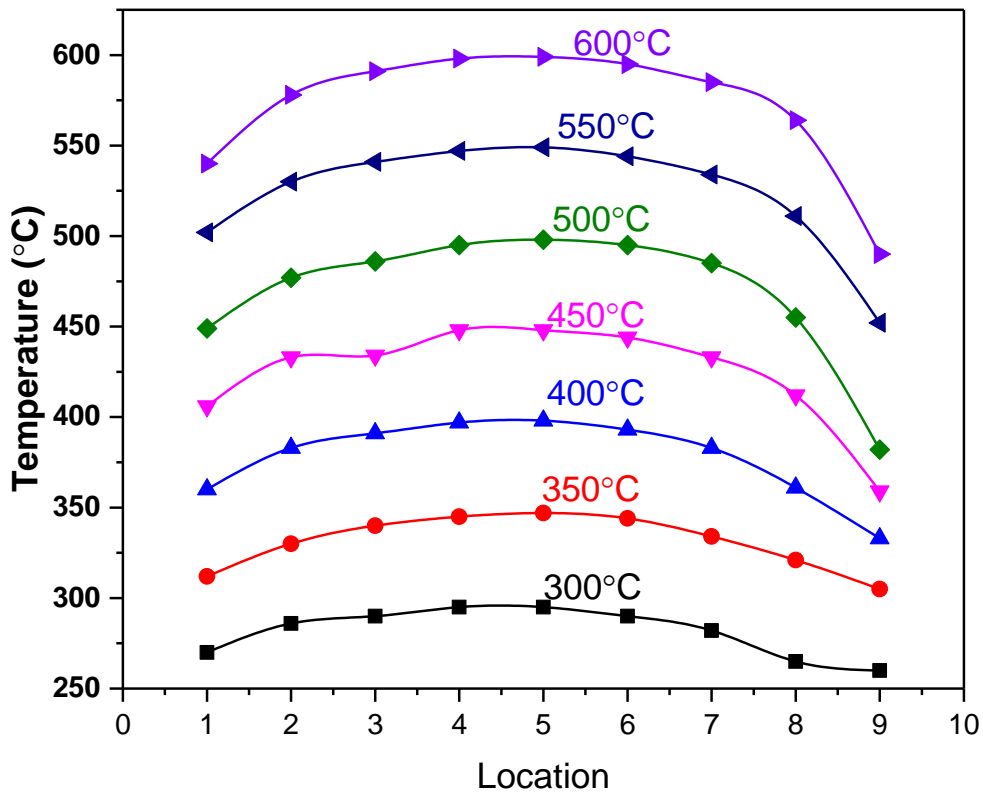
Furthermore, the experimental data of solar cell devices based on MA₃Bi₂I₉ films could also help to convince people to move eye from lab scale solution based process of MA₃Bi₂I₉ films to commercial scale APCVD process. We've tried to build solar cell device based on APCVD MA₃Bi₂I₉ films but failed to get an successful worked device, since there are too many uncertainties in the device fabrications processes.

Appendix A

The temperature profile inside the quartz chamber was captured through an Omega N-type thermocouple attached with a MAX 31856 single chip microcomputer and then linked with a customized program written in Arduino. When generating the temperature profile, all the experiment settings were the same as with the APCVD reaction except with no reactant in the chamber. The carrier gas is on, empty precursor boats were placed in the same location and the thermocouple was inserted through a home-designed flange. 2D designs were shown as follows. A diagram is shown below of the detailed setup. The insert picture along with the following code shows the attachment of the single chip microcomputer. One set of temperature profiles with 280 sccm Ar flowing is shown as follows.







The following is the code running with Arduino.

```
/*
```

```
SD card datalogger
```

```
The circuit
```

- * RTC Pin pin 10
- * MAX 31856 SCK pin 9 green
- * MAX 31856 CS pin 8 purple
- * MAX 31856 SDI pin 7 brown
- * MAX 31856 SDO pin 6 yellow

```
* MAX 31856 +V    +3.3V red
* MAX 31856 GND   ground black
* MAX 31856 DRDY  not used
* MAX 31856 FAULT not used
```

```
* thermocoupe +   orange
```

```
* thermocouple -  red
```

```
*/
```

```
#include <SD.h>
```

```
#include <Wire.h>
```

```
#include "RTClib.h"
```

```
#include "MAX31856.h"
```

```
#include <SPI.h>
```

```
#define DP 1 // No. decimal places for serial output
```

```
RTC_DS1307 rtc; //call library for clock
```

```
//assign variables for max31855
```

```
#define chipSelect 10
```

```
#define SCK      9
```

```
#define CS       8
```

```
#define SDI      7
```

```
#define SDO      6
```

```

// MAX31856 Initial settings (see MAX31856.h and the MAX31856 datasheet)

// The default noise filter is 60Hz, suitable for the USA

#define CR0_INIT (CR0_AUTOMATIC_CONVERSION +
CR0_OPEN_CIRCUIT_FAULT_TYPE_K)

#define CR1_INIT (CR1_AVERAGE_2_SAMPLES + CR1_THERMOCOUPLE_TYPE_N)

#define MASK_INIT (~(MASK_VOLTAGE_UNDER_OVER_FAULT +
MASK_THERMOCOUPLE_OPEN_FAULT))

MAX31856 *temperature;

void setup() {
  Serial.begin(57600); // Open serial communications and wait for port to open:

  #ifndef AVR
  Wire.begin();

  #endif

  rtc.begin();

  if (!rtc.isrunning()) {
    Serial.println("RTC is NOT running!");

    // following line sets the RTC to the date & time this sketch was compiled
    // This line sets the RTC with an explicit date & time, for example to set
    // January 21, 2014 at 3am you would call:

```

```
// rtc.adjust(DateTime(2014, 1, 21, 3, 0, 0));  
rtc.adjust(DateTime(F(__DATE__), F(__TIME__)));  
}
```

```
Serial.print("Initializing SD card...");
```

```
// make sure that the default chip select pin is set to output, even if you don't use it:  
pinMode(10, OUTPUT);
```

```
// see if the card is present and can be initialized:
```

```
if (!SD.begin(chipSelect)) {  
  Serial.println("Card failed, or not present");  
  // don't do anything more:  
  return;  
}
```

```
Serial.println("card initialized.");
```

```
Serial.println("MAX31856 test");
```

```
// wait for MAX chip to stabilize
```

```
delay(1000);
```

```
// Define the pins used to communicate with the MAX31856
```

```
temperature = new MAX31856(SDI, SDO, CS, SCK);
```



```

// Initializing the MAX31855's registers

temperature->writeRegister(REGISTER_CR0, CR0_INIT);

temperature->writeRegister(REGISTER_CR1, CR1_INIT);

temperature->writeRegister(REGISTER_MASK, MASK_INIT);

}

void loop(){

    DateTime now = rtc.now();

    //print date & time to serial

    Serial.print(now.year(), DEC);

    Serial.print('/');

    Serial.print(now.month(), DEC);

    Serial.print('/');

    Serial.print(now.day(), DEC);

    Serial.print(' ');

    Serial.print(now.hour(), DEC);

    Serial.print(':');

    Serial.print(now.minute(), DEC);

    Serial.print(':');

    Serial.print(now.second(), DEC);

    Serial.println();

```

```

doOver: //reset to here if tc reading is nan

float t;

float tj;

// Display the junction (IC) temperature to serial
tj = temperature->readJunction(CELSIUS);
Serial.print("Junction (IC) temperature =");
printTemperature(t);

// Display the thermocouple temperature to serial
t = temperature->readThermocouple(CELSIUS);
Serial.print(" Thermocouple temperature = ");
printTemperature(t);

Serial.println();

// Open new file on the SD Card and Begin Logging Data
File dataFile = SD.open("datalog.txt", FILE_WRITE); // open the file

if (dataFile) { // if the file is available, write to it:

    DateTime now = rtc.now(); //variable to store data/time

    //write date & time to SD card

```

```
dataFile.print(now.year(), DEC);  
dataFile.print('/');  
dataFile.print(now.month(), DEC);  
dataFile.print('/');  
dataFile.print(now.day(), DEC);  
dataFile.print(' ');  
dataFile.print(now.hour(), DEC);  
dataFile.print(':');  
dataFile.print(now.minute(), DEC);  
dataFile.print(':');  
dataFile.print(now.second(), DEC);  
dataFile.println();
```

```
//write temp to SD card
```

```
dataFile.print("C = ");
```

```
dataFile.println(t);
```

```
dataFile.close();
```

```
// print to the serial port too:
```

```
Serial.println();
```

```
}
```

```
// if the file isn't open, pop up an error:
```

```
else {
```

```
Serial.println("error opening datalog.txt");
```

```

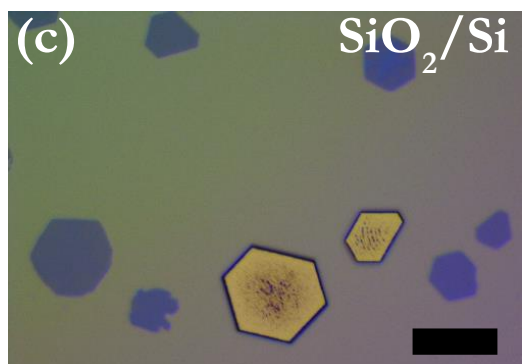
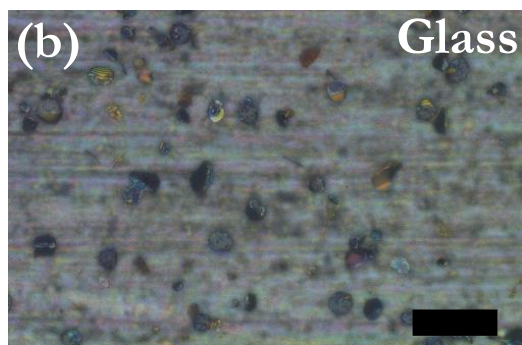
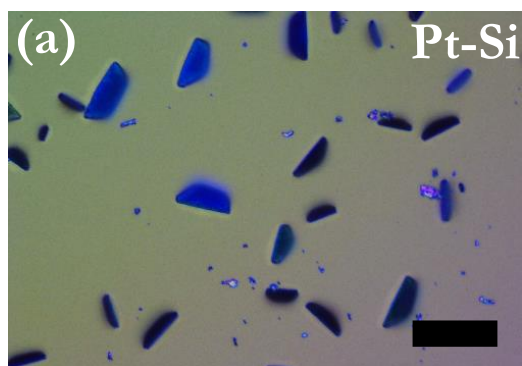
    }
    delay(1000);
}

// Print the temperature, or the type of fault
void printTemperature(double temperature) {
    switch ((int) temperature) {
        case FAULT_OPEN:
            Serial.print("FAULT_OPEN");
            break;
        case FAULT_VOLTAGE:
            Serial.print("FAULT_VOLTAGE");
            break;
        case NO_MAX31856:
            Serial.print("NO_MAX31856");
            break;
        default:
            Serial.print(temperature);
            break;
    }
    Serial.print(" ");
}

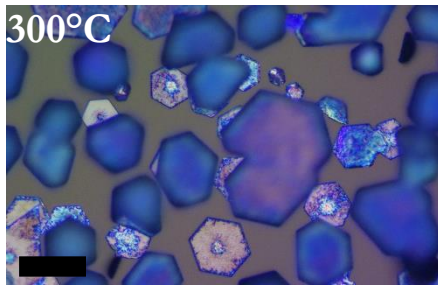
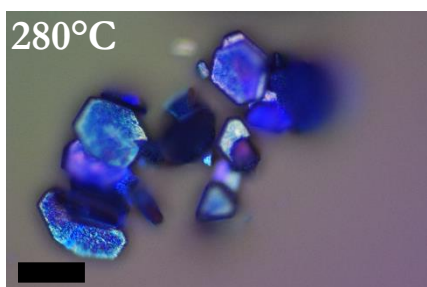
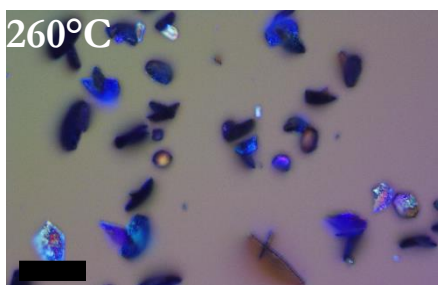
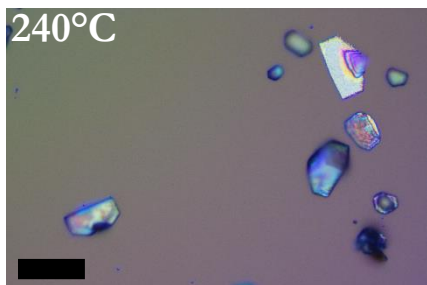
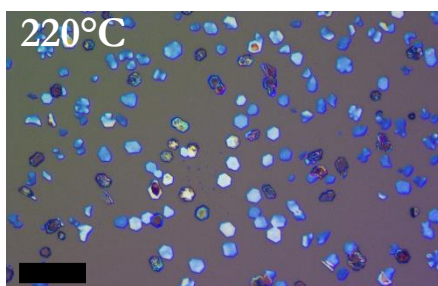
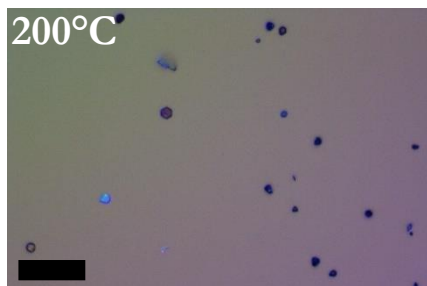
```

Appendix B

The following optical images are substrate dependent growth process of BiI_3 nanoplates, (a) is on Platinum coated silicon wafer, (b) is on glass and (c) is Silicon wafers with a 100 nm thermal oxide layer. Scale bar = 25 μm . From the previous report³⁹, the crystal shape of BiI_3 is hexagonal and it fully deposit and grow as hexagonal shape on silicon wafers with a 100 nm thermal oxide layer.

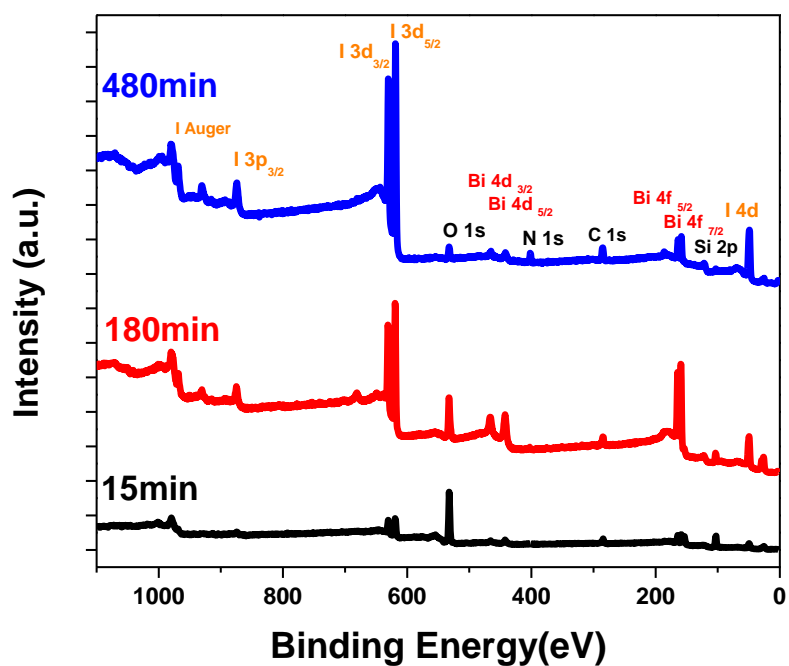


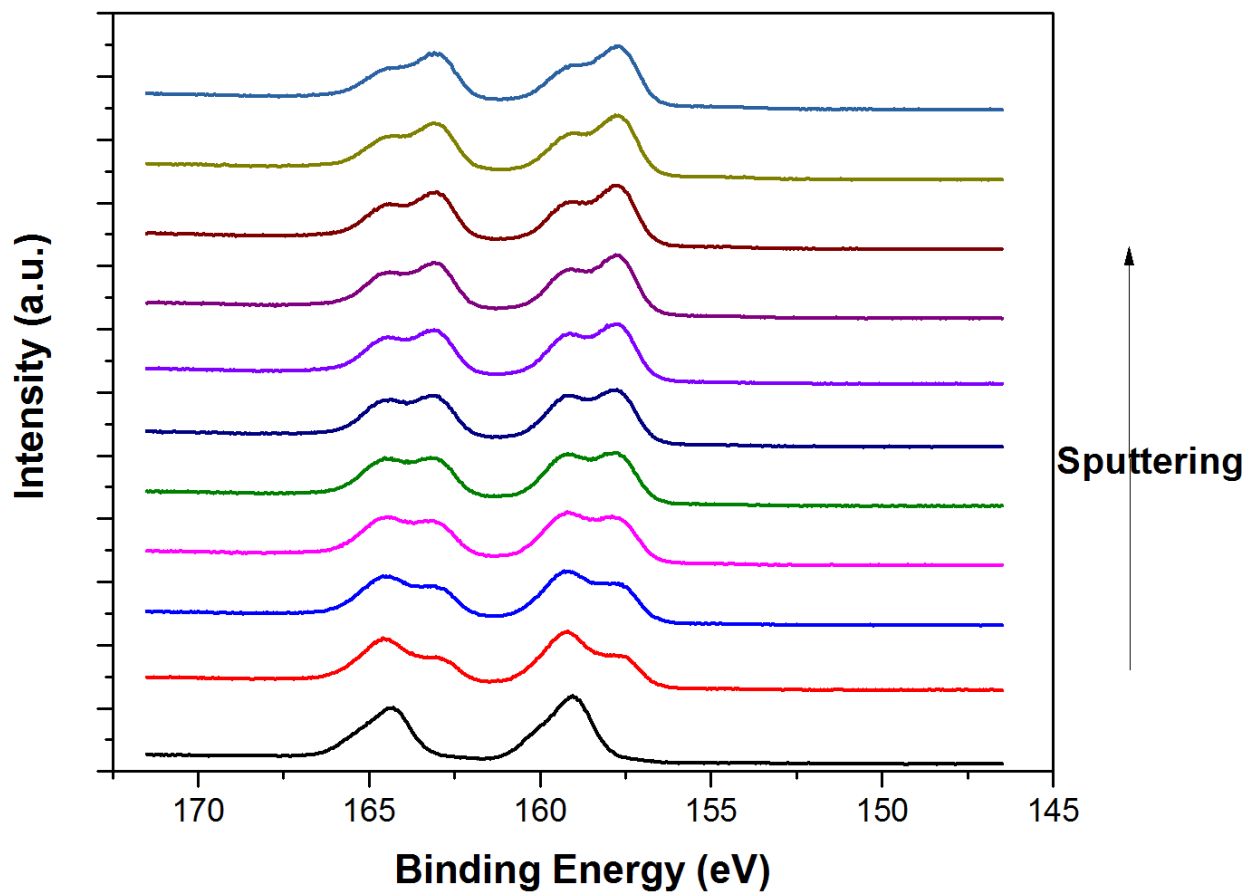
The following optical images are temperature dependent growth process of BiI₃ nanoplates. The reaction temperature is marked on images. Scale bar = 25 μm. From the pictures, as the deposit temperature increases, the nucleation is increase at first, but decrease then with a larger crystal size. This is due to as the deposition temperature increase, the nucleation rate will increase first because of the diffusion rate increase as temperature increase; later the nucleation rate is decrease because of the energy barrier to form stable nucleus is increase. These changes imply the deposition temperature range should be 220 – 240 °C.



Appendix C

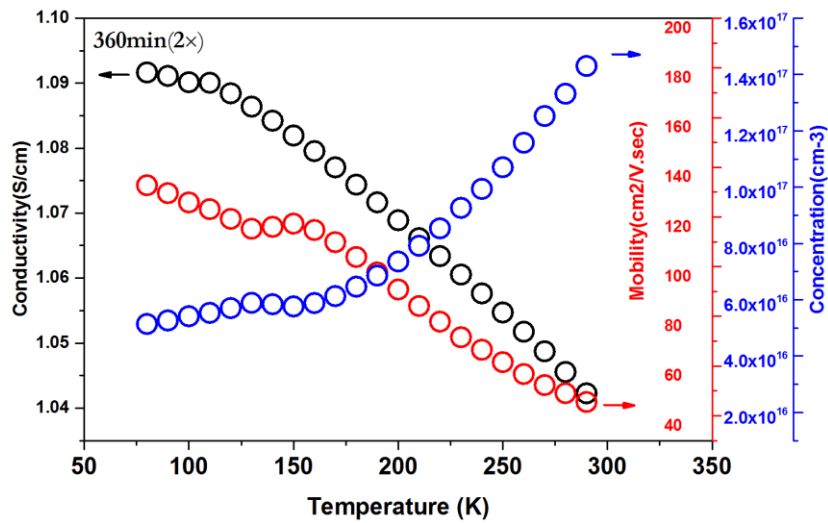
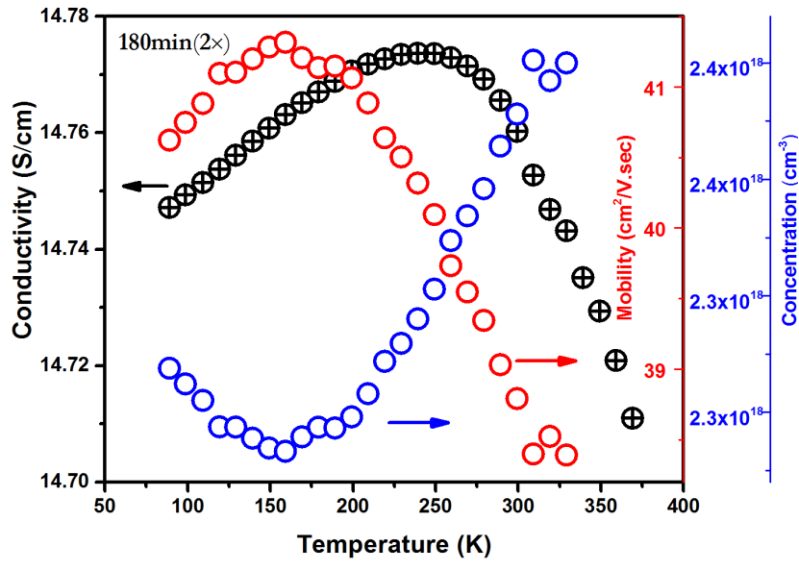
The following pictures are XPS survey spectrum and XPS depth file from Bi peak of the $\text{MA}_3\text{Bi}_2\text{I}_9$ film deposited for 15, 180 and 480 minutes. XPS survey spectrum showing Bi, I, C and N peaks, correlated to Figure 3.9.





Appendix D

The following pictures are various temperature Hall measurements of the $\text{MA}_3\text{Bi}_2\text{I}_9$ film for 180 minutes deposit twice ($2\times$) and 360 minutes deposit twice ($2\times$).



References

1. A. Kojima, K. Teshima, Y. Shirai and T. Miyasaka, *J. Am. Chem. Soc.*, 2009, **131**, 6050-6051.
2. W. S. Yang, B.-W. Park, E. H. Jung, N. J. Jeon, Y. C. Kim, D. U. Lee, S. S. Shin, J. Seo, E. K. Kim, J. H. Noh and S. I. Seok, *Science*, 2017, **356**, 1376-1379.
3. C. Wehrenfennig, G. E. Eperon, M. B. Johnston, H. J. Snaith and L. M. Herz, *Adv. Mater.*, 2014, **26**, 1584-1589.
4. J.-H. Im, C.-R. Lee, J.-W. Lee, S.-W. Park and N.-G. Park, *Nanoscale*, 2011, **3**, 4088-4093.
5. J. H. Noh, S. H. Im, J. H. Heo, T. N. Mandal and S. I. Seok, *Nano Lett.*, 2013, **13**, 1764-1769.
6. S. D. Stranks, G. E. Eperon, G. Grancini, C. Menelaou, M. J. Alcocer, T. Leijtens, L. M. Herz, A. Petrozza and H. J. Snaith, *Science*, 2013, **342**, 341-344.
7. G. Xing, N. Mathews, S. Sun, S. S. Lim, Y. M. Lam, M. Grätzel, S. Mhaisalkar and T. C. Sum, *Science*, 2013, **342**, 344-347.
8. B. W. Park, B. Philippe, X. Zhang, H. Rensmo, G. Boschloo and E. M. Johansson, *Adv. Mater.*, 2015, **27**, 6806-6813.
9. A. Kulkarni, T. Singh, M. Ikegami and T. Miyasaka, *RSC Advances*, 2017, **7**, 9456-9460.
10. M. Lyu, J.-H. Yun, M. Cai, Y. Jiao, P. V. Bernhardt, M. Zhang, Q. Wang, A. Du, H. Wang, G. Liu and L. Wang, *Nano Res.*, 2016, **9**, 692-702.
11. K. Eckhardt, V. Bon, J. Getzschmann, J. Grothe, F. M. Wisser and S. Kaskel, *Chem. Commun.*, 2016, **52**, 3058-3060.
12. R. L. Hoyer, R. E. Brandt, A. Osherov, V. Stevanović, S. D. Stranks, M. W. Wilson, H. Kim, A. J. Akey, J. D. Perkins and R. C. Kurchin, *Chem. Eur. J.*, 2016, **22**, 2605-2610.
13. T. Okano and Y. Suzuki, *Mater. Lett.*, 2017, **191**, 77-79.
14. M. Liu, M. B. Johnston and H. J. Snaith, *Nature*, 2013, **501**, 395-398.

15. Y. X. Zhao and K. Zhu, *J. Phys. Chem. Lett.*, 2014, **5**, 4175-4186.
16. M. J. Madou, *Fundamentals of microfabrication: the science of miniaturization*, CRC press, 2002.
17. T. D. Manning, I. P. Parkin, R. J. Clark, D. Sheel, M. E. Pemble and D. Vernadou, *J. Mater. Chem.*, 2002, **12**, 2936-2939.
18. T. D. Manning, I. P. Parkin, M. E. Pemble, D. Sheel and D. Vernadou, *Chem. Mater.*, 2004, **16**, 744-749.
19. S. A. Campbell, S. A. Campbell and A. C. Stephen, *Fabrication engineering at the micro-and nanoscale*, 2008.
20. W. Kern, *Thin film processes II*, Academic press, 2012.
21. N. Ahn, D.-Y. Son, I.-H. Jang, S. M. Kang, M. Choi and N.-G. Park, *J. Am. Chem. Soc.*, 2015, **137**, 8696-8699.
22. T. M. Brenner, Y. Rakita, Y. Orr, E. Klein, I. Feldman, M. Elbaum, D. Cahen and G. Hodes, *Chem. Mater.*, 2016, **28**, 6501-6510.
23. J. Burschka, N. Pellet, S.-J. Moon, R. Humphry-Baker, P. Gao, M. K. Nazeeruddin and M. Grätzel, *Nature*, 2013, **499**, 316-319.
24. J. Chen, J. Xu, L. Xiao, B. Zhang, S. Y. Dai and J. X. Yao, *ACS Appl. Mater. Interfaces*, 2017, **9**, 2449-2458.
25. X. M. Chen, H. Q. Cao, H. Yu, H. Zhu, H. P. Zhou, L. Y. Yang and S. G. Yin, *J. Mater. Chem. A*, 2016, **4**, 9124-9132.
26. M. I. El-Henawey, R. S. Gebhardt, M. M. El-Tonsy and S. Chaudhary, *J. Mater. Chem. A*, 2016, **4**, 1947-1952.
27. Y. Li, J. K. Cooper, R. Buonsanti, C. Giannini, Y. Liu, F. M. Toma and I. D. Sharp, *J. Phys. Chem. Lett.*, 2015, **6**, 493-499.
28. J. C. S. Costa, J. Azevedo, L. Santos and A. Mendes, *J. Phys. Chem. C*, 2017, **121**, 2080-2087.
29. P. Fan, D. Gu, G. X. Liang, J. T. Luo, J. L. Chen, Z. H. Zheng and D. P. Zhang, *Sci Rep*, 2016, **6**.

30. M. R. Leyden, Y. Jiang and Y. B. Qi, *J. Mater. Chem. A*, 2016, **4**, 13125-13132.
31. C. W. Chen, H. W. Kang, S. Y. Hsiao, P. F. Yang, K. M. Chiang and H. W. Lin, *Adv. Mater.*, 2014, **26**, 6647-6652.
32. C. Y. Chen, H. Y. Lin, K. M. Chiang, W. L. Tsai, Y. C. Huang, C. S. Tsao and H. W. Lin, *Adv. Mater.*, 2017, **29**.
33. M. M. Tavakoli, L. L. Gu, Y. Gao, C. Reckmeier, J. He, A. L. Rogach, Y. Yao and Z. Y. Fan, *Sci Rep*, 2015, **5**.
34. A. Dualeh, P. Gao, S. I. Seok, M. K. Nazeeruddin and M. Grätzel, *Chem. Mater.*, 2014, **26**, 6160-6164.
35. Y. Myung, F. Wu, S. Banerjee, A. Stoica, H. Zhong, S.-S. Lee, J. Fortner, L. Yang and P. Banerjee, *Chem. Mater.*, 2015, **27**, 7710-7718.
36. A. Cuña, I. Aguiar, A. Gancharov, M. Pérez and L. Fornaro, *Cryst. Res. Technol.*, 2004, **39**, 899-905.
37. M. T. Vieyra-Eusebio and A. Rojas, *J. Chem. Eng. Data.*, 2011, **56**, 5008-5018.
38. I. Langmuir, *Phys. Rev.*, 1913, **2**, 329.
39. D. Nason and L. Keller, *J. Cryst. Growth*, 1995, **156**, 221-226.
40. S. Öz, J.-C. Hebig, E. Jung, T. Singh, A. Lepcha, S. Olthof, F. Jan, Y. Gao, R. German and P. H. van Loosdrecht, *Sol. Energy Mater. Sol. Cells*, 2016, **158**, 195-201.
41. M. Vigneshwaran, T. Ohta, S. Iikubo, G. Kapil, T. S. Ripolles, Y. Ogomi, T. Ma, S. S. Pandey, Q. Shen and T. Toyoda, *Chem. Mater.*, 2016, **28**, 6436-6440.
42. T. Singh, A. Kulkarni, M. Ikegami and T. Miyasaka, *ACS Appl. Mater. Interfaces*, 2016, **8**, 14542-14547.
43. K. M. Boopathi, S. Raman, R. Mohanraman, F.-C. Chou, Y.-Y. Chen, C.-H. Lee, F.-C. Chang and C.-W. Chu, *Sol. Energy Mater. Sol. Cells*, 2014, **121**, 35-41.
44. M. Abulikemu, S. Ould-Chikh, X. Miao, E. Alarousu, B. Murali, G. O. N. Ndjawa, J. Barbé, A. El Labban, A. Amassian and S. Del Gobbo, *J. Mater. Chem. A*, 2016, **4**, 12504-12515.

45. M. E. Kamminga, A. Stroppa, S. Picozzi, M. Chislov, I. A. Zvereva, J. Baas, A. Meetsma, G. R. Blake and T. T. Palstra, *Inorg. Chem.*, 2017, **56**, 33-41.
46. M. Scholz, O. Flender, K. Oum and T. Lenzer, *J. Phys. Chem. C*, 2017.
47. C. Ran, Z. Wu, J. Xi, F. Yuan, H. Dong, T. Lei, X. He and X. Hou, *J Phys Chem Lett*, 2017, **8**, 394-400.
48. A. J. Lehner, D. H. Fabini, H. A. Evans, C.-A. Hébert, S. R. Smock, J. Hu, H. Wang, J. W. Zwanziger, M. L. Chabinyk and R. Seshadri, *Chem. Mater.*, 2015, **27**, 7137-7148.
49. L. Liu, J. A. McLeod, R. Wang, P. Shen and S. Duhm, *Appl. Phys. Lett.*, 2015, **107**, 061904.
50. M. Abulikemu, S. Ould-Chikh, X. Miao, E. Alarousu, B. Murali, G. O. Ngongang Ndjawa, J. Barbé, A. El Labban, A. Amassian and S. Del Gobbo, *J. Mater. Chem. A*, 2016, **4**, 12504-12515.
51. T. Kawai, A. Ishii, T. Kitamura, S. Shimanuki, M. Iwata and Y. Ishibashi, *J. Phys. Soc. Jpn.*, 1996, **65**, 1464-1468.
52. M. Scholz, O. Flender, K. Oum and T. Lenzer, *J. Phys. Chem. C*, 2017, **121**, 12110-12116.
53. S. Öz, J.-C. Hebig, E. Jung, T. Singh, A. Lepcha, S. Olthof, F. Jan, Y. Gao, R. German, P. H. M. van Loosdrecht, K. Meerholz, T. Kirchartz and S. Mathur, *Sol. Energy Mater. Sol. Cells*, 2016, **158**, 195-201.
54. J. I. Pankove, *Optical processes in semiconductors*, Courier Corporation, 2012.
55. M. E. Kamminga, A. Stroppa, S. Picozzi, M. Chislov, I. A. Zvereva, J. Baas, A. Meetsma, G. R. Blake and T. T. M. Palstra, *Inorg. Chem.*, 2017, **56**, 33-41.
56. Y. Li, X. Xu, C. Wang, C. Wang, F. Xie, J. Yang and Y. Gao, *J. Mater. Chem. C*, 2015, **119**, 23996–24002.
57. J. Chastain, R. C. King and J. Moulder, *Handbook of X-ray photoelectron spectroscopy: a reference book of standard spectra for identification and interpretation of XPS data*, Physical Electronics Division, Perkin-Elmer Corporation Eden Prairie, Minnesota, 1992.
58. X.-j. Wang, F.-t. Li, D.-y. Li, R.-h. Liu and S.-j. Liu, *Mater. Sci. Eng., B-Adv.*, 2015, **193**, 112-120.

59. H. Liu, W. R. Cao, Y. Su, Y. Wang and X. H. Wang, *Appl. Catal., B*, 2012, **111**, 271-279.

Vita

Xiao Chen

6136 Delmar Blvd, Apt 301, St Louis, MO 63112 | (314)312-8290 | chenxiao@wustl.edu

SUMMARY

Thesis based Master candidate in Materials Science & Engineering with extensive lab experience seeks an Engineer position to apply my leading lab techniques to real life applications. Fluent Mandarin and English. Willing to travel and relocate.

EDUCATION

Washington University in St. Louis | 08/2017

Master: Materials Science Engineering
Lab for Emerging and Applied Nanomaterials

Sichuan University | 06/2015

Bachelor: Inorganic and Non-metallic Materials
Science Engineering

SKILLS

Laboratory: Advanced operator of Sputtering, SEM, EDS, XRD, FT-IR and UV-VIS; licensed user of XPS, UPS, AFM and Raman Microscope; experienced in JANIS (electrical property test probe station) and EC-LAB.

Cleanroom: RIE and Wet Etch, Photolithography, Ellipsometry, Profilometer, Spin Coater, PVD, Oxidation Furnace

Software: Proficient in Origin, ImageJ, and Microsoft Office; Familiar with Auto CAD, Inventor, and MATLAB

Languages: Fluent in Mandarin and English

ENGINEER EXPERIENCE

Research Assistant | Wash U Lab for Emerging and Applied Nanomaterials | 01/2016-present

Single-step vapor phase deposition of organic/inorganic perovskite thin films

- Invented optimal procedure to synthesize organic/inorganic thin films through chemical vapor depositions
- Designed and produced a flange to assemble thermocouples in the CVD system
- Supervised 2 undergraduates to create programs to retrieve and build temperature model of CVD system
- Characterized the morphology, optical, electrical properties of perovskite films
- Designed and produced a perovskite solar cell

Team Member | Wash U Institute of Materials Science & Engineering | 01/2016-05/2016

Comb shape Au-Al bi-electrode ZnO UV sensor

- Designed comb shape bi-electrode photolithography mask through Auto CAD
- Fabricated UV sensors in cleanroom, techniques involved thermal evaporator, PVD, and RIE.
- Examined qualities, conductivities, stabilities, sensitivities and recoveries of devices through probe station

Team Leader | Sichuan University | 03/2012-03/2014

Thermoelectric properties of Co-based oxide thermoelectric ceramic

- Prepared Ca-Co-O-based thermoelectric ceramics using sol-gel and chemical co-precipitation methods and formed the thermoelectric ceramics with dry pressing and isostatic cool pressing
- Characterized the morphology, thermal conductivity and electrical conductivity
- Investigated the thermoelectric properties of ceramics synthesized by different methods to obtain better thermoelectric performance
- Supported by University Training Program of Innovation and Entrepreneurship for Undergraduates

ADDITIONAL EXPERIENCE

Graduate Teaching Fellow | Wash U Department of Mechanical Eng. & Materials Science | 09/2016-present

- Electronic Materials Processing | 01/2017-present
- Quantitative Materials Science Engineering | 09/2016-12/2016